

Sidekick 2 directs formation of a retinal circuit that detects differential motion

Arjun Krishnaswamy^{1*}, Masahito Yamagata^{1*}, Xin Duan¹, Y. Kate Hong^{1†} & Joshua R. Sanes¹

In the mammalian retina, processes of approximately 70 types of interneurons form specific synapses on roughly 30 types of retinal ganglion cells (RGCs) in a neuropil called the inner plexiform layer. Each RGC type extracts salient features from visual input, which are sent deeper into the brain for further processing^{1–4}. The specificity and stereotypy of synapses formed in the inner plexiform layer account for the feature-detecting ability of RGCs. Here we analyse the development and function of synapses on one mouse RGC type, called the W3B-RGC^{5,6}. These cells have the remarkable property of responding when the timing of the movement of a small object differs from that of the background, but not when they coincide⁶. Such cells, known as local edge detectors or object motion sensors, can distinguish moving objects from a visual scene that is also moving^{6–12}. We show that W3B-RGCs receive strong and selective input from an unusual excitatory amacrine cell type

known as VG3-AC (vesicular glutamate transporter 3). Both W3B-RGCs and VG3-ACs express the immunoglobulin superfamily recognition molecule sidekick 2 (Sd2)^{13,14}, and both loss- and gain-of-function studies indicate that Sd2-dependent homophilic interactions are necessary for the selectivity of the connection. The Sd2-specified synapse is essential for visual responses of W3B-RGCs: whereas bipolar cells relay visual input directly to most RGCs, the W3B-RGCs receive much of their input indirectly, via the VG3-ACs. This non-canonical circuit introduces a delay into the pathway from photoreceptors in the centre of the receptive field to W3B-RGCs, which could improve their ability to judge the synchrony of local and global motion.

In situ hybridization revealed that both *Sdk1* and *Sdk2* were expressed in subsets of mouse retinal neurons (Fig. 1a–c). *Sdk1*- and *Sdk2*-positive cells were largely non-overlapping, as shown previously

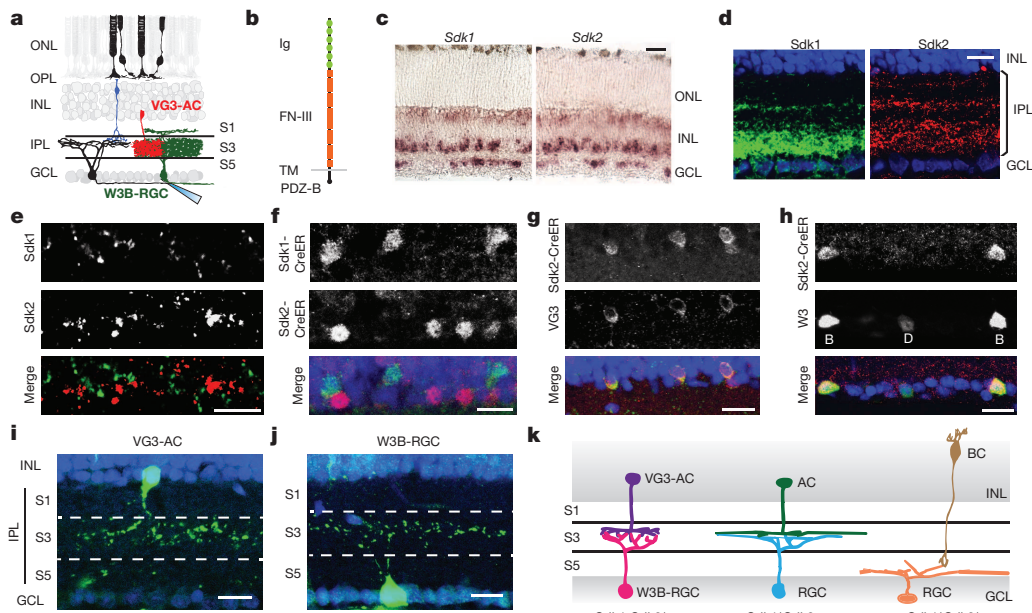


Figure 1 | Sidekick proteins are expressed by subsets of retinal neurons.

a, Photoreceptors in the outer nuclear layer (ONL) synapse on bipolar cells. Bipolar (blue), amacrine (red) and RGCs (black) synapse in the inner plexiform layer (IPL), which is divided into five sublaminae (S1–S5). W3B-RGCs are targeted for whole-cell recording and interneurons stimulated optogenetically. b, Structure of Sdk protein. FN-III, fibronectin type III domains; Ig, immunoglobulin domains; PDZ-B, PDZ-binding, synaptic-localizing sequence; TM, transmembrane domain. c, Expression of *Sdk1* and *Sdk2* in postnatal day (P) 8 retina assessed by *in situ* hybridization in retinal cross-sections. d, Immunohistochemical detection of *Sdk1* and *Sdk2* at P30. e, Double-label immunohistochemistry shows non-overlapping *Sdk1*- and

Sdk2-rich puncta in S3. f, Double-staining for epitope-tagged CreER in *Sdk1*^{cre/+} *Sdk2*^{cre/+} mouse shows largely non-overlapping expression at P30. g, VG3-ACs are *Sdk2*-positive, as shown by immunostaining for VG3 and CreER in *Sdk2*^{cre/+} mouse. h, W3B-RGCs (B) are *Sdk2*-positive (CreER and GFP double staining in *Sdk2*^{cre/+}; TYW3 mouse). Dimmer W3D-RGCs (D) are *Sdk2*-negative. i, j, A VG3-AC (i) and a W3B-RGC (j) imaged in *Sdk2*^{cre/+} mated to a reporter line. k, Arborization pattern of principal retinal cell types that express *Sdk1* and *Sdk2*. The amacrine and bipolar cell types (AC and BC) that express *Sdk1* remain to be determined. GCL, ganglion cell layer; INL, inner nuclear layer; ONL, outer nuclear layer. Scale bars, 10 μm.

¹Department of Molecular and Cellular Biology and Center for Brain Science, Harvard University, Cambridge, Massachusetts 02138, USA. [†]Present address: Department of Neuroscience, Columbia University, New York 10032, USA.

*These authors contributed equally to this work.

in chicks^{13,14}, however, a double-positive population was also present in mouse (Extended Data Fig. 1a). Expression was evident by embryonic day 17 and persisted into adulthood, spanning the periods of lamina formation and synaptogenesis (Extended Data Fig. 1b). Immunostaining showed that Sdk proteins were concentrated in the synapse-rich inner plexiform layer (IPL) (Fig. 1d), presumably owing to their carboxy-terminal synaptic localizing motif¹⁵. Sdk proteins were concentrated in two of five strata within the IPL, S3 and S5. Sdk1- and Sdk2-positive puncta in S3 were non-overlapping, consistent with the complementary expression pattern of the genes (Fig. 1e).

We generated mice in which a ligand-activated Cre recombinase (CreER) fused to distinct epitope tags was targeted to the first coding exon (*Sdk1^{ce}* and *Sdk2^{ce}*; Extended Data Fig. 2a-f). Interneurons and RGCs that expressed *Sdk1* or *Sdk2*, identified using reporter lines or immunostaining, arborized in S3; neurons that expressed both *Sdk1* and *Sdk2* arborized in S5. *Sdk1^{-/-}/Sdk2⁺* RGCs were W3B-RGCs, labelled by yellow fluorescent protein (YFP) in the TYW3 cell line, which we generated and characterized previously^{5,6}. Another set of morphologically similar RGCs, called W3D, which are dimly labelled in the TYW3 line, expressed neither *Sdk1* nor *Sdk2*. Most *Sdk1^{-/-}/Sdk2⁺* interneurons expressed the vesicular glutamate transporter 3 (VGluT3), encoded by *Slc17a8* (refs 16–18); we refer to these cells as VG3-ACs. Both W3B-RGCs and VG3-ACs extend dendrites that arborized in S3 (Fig. 1f-k and Extended Data Fig. 2g-i).

To determine whether VG3-ACs synapse on W3B-RGCs, we implemented an optogenetic strategy (Extended Data Fig. 3). We generated mice^{5,17} in which VG3-ACs expressed channelrhodopsin 2 (ChR2) fused to a red fluorescent protein, and W3B-RGCs were labelled with YFP. We targeted YFP-positive W3B-RGCs in explanted retinas with patch electrodes, and activated ChR2 in VG3-ACs using two-photon stimulation. Optogenetic stimulation of individual VG3-ACs evoked reliable postsynaptic currents in W3B-RGCs (Fig. 2a, top trace). Displacement of the laser (~10 µm) so that it was within the receptive field of the RGC but no longer illuminated a ChR2-expressing cell evoked no stimulus-locked current (Fig. 2a, bottom trace). Thus, responses were due to excitation of ChR2 rather than photoreceptors. Additional physiological and pharmacological studies demonstrated that VG3-ACs formed excitatory, glutamatergic connections on RGCs (Extended Data Fig. 4a-c), consistent with recent studies of VGluT3-containing neurons in retina^{19,20} and other brain areas²¹.

We devised a test to determine whether the VG3-AC-W3B-RGC connection was monosynaptic. Although the light-activated ion channel ChR2 is highly calcium permeable, we found that it is insensitive to CdCl₂, a blocker of endogenous voltage-activated calcium channels in nerve terminals (Extended Data Fig. 4d-h). Thus, in the presence of CdCl₂, neurotransmitter can be released only from ChR2-positive terminals. Synaptic currents elicited by activating terminal arbors of ChR2-expressing VG3-ACs persisted in the presence of CdCl₂ (Extended Data Fig. 4i-k). Gap junction blockers had no effect on these currents, ruling out the possibility that calcium entering through ChR2 in VG3-ACs permeated gap junctions to electrically coupled glutamatergic bipolar cells, which then synapsed on W3B-RGCs (Extended Data Fig. 4b). Together, these results demonstrate that VG3-ACs form synapses directly on W3B-RGCs.

To assess convergence of VG3-ACs onto W3B-RGCs, we recorded from W3B-RGCs while stimulating 60–200 VG3-ACs within 200 µm of their somata. All VG3-ACs and W3B-RGCs separated by ≤100 µm were connected, with the strength of the connection inversely proportional to the distance between them (Fig. 2b). Because the radii of VG3-ACs and W3B-RGCs dendritic arbors are ~25 µm and ~60 µm, respectively^{5,17,19,20}, we conclude that VG3-ACs are functionally connected to W3B-RGCs whenever their dendrites overlap (Fig. 2c).

The strong connectivity of VG3-ACs to W3B-RGCs could be a simple consequence of the overlap of their arbors^{22–24}, as predicted by Peters' rule, which posits that connectivity is proportional to the proximity of pre- and postsynaptic arbors^{22–25}. To test this idea, we

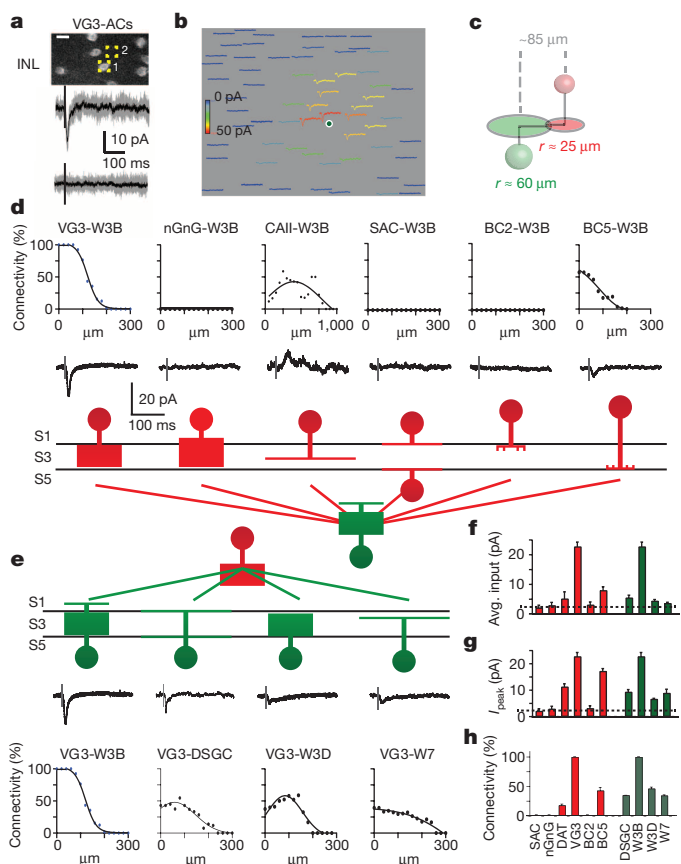


Figure 2 | Selective connectivity of VG3-ACs and W3B-RGCs. **a**, Current recorded from a W3B-RGC after optogenetic stimulation of a VG3-AC (top trace); no current is recorded when the stimulus is displaced by ~10 µm (bottom trace). Grey traces denote 10 trials, black traces show the average. Scale bar, 10 pA, 100 ms. **b**, Currents recorded in W3B-RGCs in response to stimulating 64 VG3-ACs in a 250 × 200 µm grid enclosing the RGC. Heat map indicates peak strength of connections; position of trace corresponds to position of stimulated VG3-AC soma. **c**, Cartoon showing the radii of VG3-AC and W3B-RGC arbors, indicating distance over which overlap occurs. **d**, **e**, Strength of connections as a function of distance from six interneuron types to W3B-RGCs (**d**) and from VG3-ACs to four RGC types (**e**). Sample currents shown below each graph. The W7 population contained six nearly disconnected and ten connected pairs, presumably corresponding to the S1-laminating and S3-laminating W7 subsets. Full data are shown in Extended Data Fig. 5. Upward currents are inhibitory (holding potential (V_h) ≈ 0 mV); downward currents are excitatory (V_h ≈ -60 mV). BC2, type 2 bipolar cells; BC5, type 5 bipolar cells; CAII, type II catecholaminergic cells. **f**, Average strength of connectivity for pairs shown in **d**, **g**, Strength of connections (average peak current, I_{peak}) for pairs in which responses exceeded baseline (dotted line, average noise floor, 2–3 pA). V_h = -70 mV for inward currents, and -10 mV for outward currents. **h**, Percentage of connected pairs for VG3-AC to RGC recordings and interneuron to W3B-RGC recordings averaged over 100 µm radius from the postsynaptic RGC. Full data and n values for **f–h** are shown in Extended Data Fig. 5. Error bars in **f–h** denote mean ± s.e.m.

measured the connectivity of VG3-ACs to four Sdk2-negative RGC types for which we had marker lines: W3D-RGCs, W7-RGCs and two types of ON-OFF direction-selective RGCs (ooDSGCs); W3D-RGC and W7-RGC dendrites intermingle with those of W3B-RGCs, and ooDSGC dendrites straddle those of W3B-RGCs. Optogenetic stimulation of VG3-ACs elicited excitatory postsynaptic currents from W3D-RGCs, W7-RGCs and ooDSGCs that were qualitatively similar to, but only ~10% as strong as those in W3B-RGCs (Fig. 2e, f and Extended Data Fig. 5). The weakness resulted from a twofold decrease in the fraction of pairs that were detectably connected, and a fivefold decrease in the peak synaptic currents for connected pairs (Fig. 2g, h).

We also assayed input to W3B-RGCs from six other types of interneurons that arborize in or at the border of S3. In all cases, connectivity was many-fold lower than that between VG3-ACs and W3B-RGCs (Fig. 2d–h). Together, these data demonstrate that Peters' rule is insufficient to explain patterns of connectivity in the neuropil of the retina.

To address whether *Sdk2* is involved in the establishment of the strong VG3-AC to W3B-RGC connection, we used the *Sdk2^{ce/ce}* line, in which insertion of CreER generates a *Sdk2*-null allele (Extended Data Fig. 2). *Sdk2^{ce/ce}* mice are viable, fertile and exhibit no external deficits. We detected no alterations in retinal structure or in the numbers or positions of any cell types examined (Extended Data Fig. 6). However, physiological analysis revealed a 20-fold reduction in the strength of synaptic connections between VG3-ACs and W3B-RGCs (Fig. 3a–d). Thus, *Sdk2* is required for the selective connectivity of VG3-ACs to W3B-RGCs.

We sought morphological correlates of the synaptic disruption observed in *Sdk2* mutants. To this end, we imaged single VG3-ACs and W3B-RGCs labelled in a transgenic line or by dye injection. The size, shape and laminar restriction of VG3-AC and W3B-RGC arbors were generally normal in *Sdk2^{ce/ce}* mice (Fig. 3e, f). However, branch number and length were modestly reduced in mutant W3B-RGCs and modestly increased in VG3-ACs; in both cell types, some branches extended beyond the normal termination zone (Fig. 3g–l and Extended Data Figs 6m–o and 7). Defects in laminar restriction were similar to, although less striking than, those observed in chick retina after microRNA-mediated attenuation of *Sdk2* (ref. 13). In chicks, *SDK2* expression was decreased in isolated cells in a wild-type background; we speculate that this led to competition between normal and mutant neurons resulting in greater defects than observed in the null mouse mutant.

The result that *Sdk2*-positive neurons connect more strongly to each other than to *Sdk2*-negative partners is consistent with the finding that *Sdk* proteins are homophilic adhesion molecules^{12,13}. If this is true, defects should be observed only at synapses in which both partners express *Sdk2*. To test this idea, we asked whether *Sdk2* deletion affected synapses in which only one partner was *Sdk2*-positive. Deletion of *Sdk2* had no effect on the strength of coupling in any of four such cases: connections of *Sdk2*-negative bipolar and amacrine cells to W3B-RGCs and of VG3-ACs to *Sdk2*-negative RGCs (Fig. 3b–d and Extended Data Fig. 8a–r). These results also provide evidence that loss of *Sdk2* does not affect the overall properties of VG3-ACs or W3B-RGCs. In addition, we generated mice in which *Sdk2* could be expressed in a Cre-dependent manner in any cell (Extended Data Fig. 8s). In combination with the *Sdk2^{ce/ce}* line, this allowed us to restore *Sdk2* in VG3-ACs selectively. In this case, connectivity was as low as in the *Sdk2^{ce/ce}* mutants (Extended Data Fig. 8t). Together, these results support the idea that *Sdk2* promotes connectivity by a homophilic mechanism.

We next asked what role the *Sdk2*-specified VG3-AC-to-W3B-RGC connection has in the function of W3B-RGCs. To this end, we recorded responses of W3B-RGCs to visual rather than optogenetic stimulation. As reported previously^{5,6,20}, a bright spot flashed over the dendritic arbor (the receptive field centre) of control W3B-RGCs elicited a burst of action potentials at both the onset and the offset of the light, with the OFF response substantially larger than the ON response. In *Sdk2^{ce/ce}* mice, the ON response persisted but the OFF response was nearly abolished (Fig. 4a and Extended Data Fig. 9a). This result was unexpected, because input from amacrine cells generally modulates RGC responses but does not generate them³. To address whether this phenotype resulted from decreased excitation or enhanced inhibition, we recorded synaptic currents in response to the same stimulus. Consistent with results from the voltage recording, a flashing spot elicited excitatory currents at both light onset and offset, with OFF currents larger than ON currents; in *Sdk2* mutants, the OFF current was nearly abolished while the ON current was less affected (Fig. 4c, d). By contrast, inhibitory currents evoked in W3B-RGCs by full-field

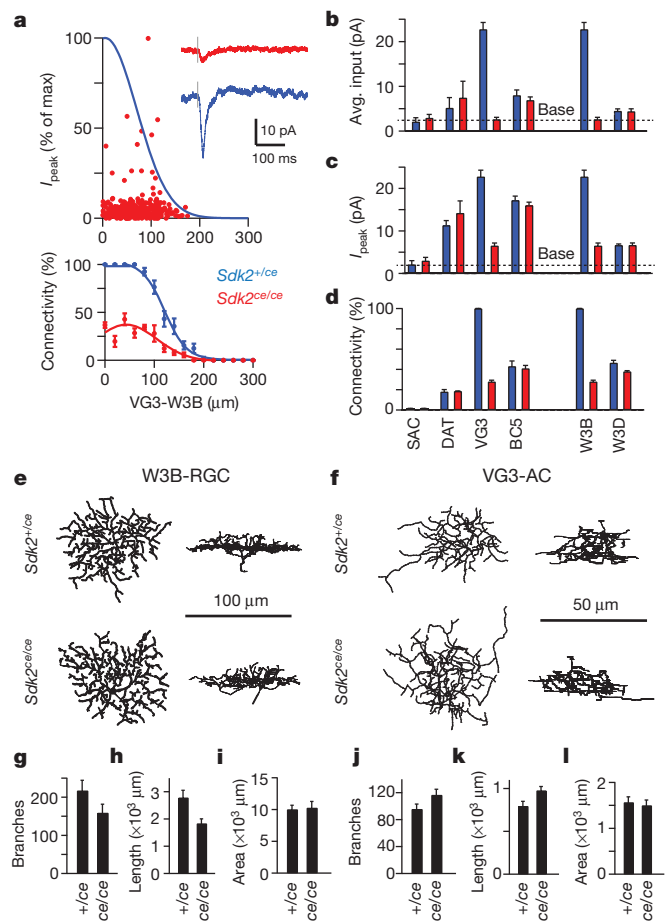


Figure 3 | Decreased synaptic connectivity in *Sdk2* mutants. **a**, Strength of connections from VG3-ACs to W3B-RGCs in *Sdk2^{ce/ce}* mutants, derived from 557 VG3-ACs and 12 W3B-RGCs. Fit to the control data (Extended Data Fig. 5a) re-plotted in blue. Inset, VG3-AC-evoked currents recorded from a W3B-RGC in *Sdk2^{ce/ce}* and *Sdk2^{ce/+}* retinas. **b–d**, Synaptic connectivity in *Sdk2^{ce/ce}* mutants and those in controls. Graphs show total strength of connections (**b**), strength of connections for pairs in which responses exceeded baseline (**c**, dotted line) and percentage of connected pairs (**d**). Full data are shown in Extended Data Fig. 8. **e, f**, En face and laminar projections of skeletonized dendritic arbors from dye-filled W3B-RGCs (**e**) or VG3-ACs (**f**) labelled sparsely with tdTomato in *Sdk2^{ce/ce}* and *Sdk2^{ce/+}* retinas. **g–i**, Average branch number, branch length, and dendritic field area for W3B-RGCs in *Sdk2^{ce/ce}* and *Sdk2^{ce/+}* retinas. Data from 14 W3B-RGCs in 8 *Sdk2^{ce/ce}* mice and 11 W3B-RGCs in 9 *Sdk2^{ce/ce}* mice. **j–l**, Similar to **g–i**, except for 9 VG3-ACs in 6 *Sdk2^{ce/ce}* mice and 10 VG3-ACs in 8 *Sdk2^{ce/ce}* mice. Data in **b–d** and **g–l** indicate mean \pm s.e.m.

stimulation, presumably derived from conventional amacrine cells, were unaffected in *Sdk2* mutants (Fig. 4e and Extended Data Fig. 9b). The effect was specific in that light-evoked inward currents in neighbouring RGCs, such as W3D-RGCs, persisted in *Sdk2* mutants (Extended Data Fig. 9c).

The effect we observed could have resulted from defects in other *Sdk2*-expressing retinal cells (Fig. 1k), or compensatory alterations during development. To test these possibilities, we selectively ablated mature VG3-ACs. We expressed the diphtheria toxin receptor (DTR) in VG3-ACs, injected diphtheria toxin in adult animals, recorded from W3B-RGCs ~10 days after injection, and verified loss of VG3-ACs after recording (Extended Data Fig. 9d, e). Ablation of VG3-ACs in adulthood led to an even greater loss of light-evoked excitatory OFF responses than observed after global deletion of *Sdk2*; inhibitory responses in W3B-RGCs and excitatory responses in nearby RGCs were unaffected (Fig. 4e, g and Extended Data Fig. 9f–h; see also ref. 20). Together, these results lead to the conclusion that visual input are

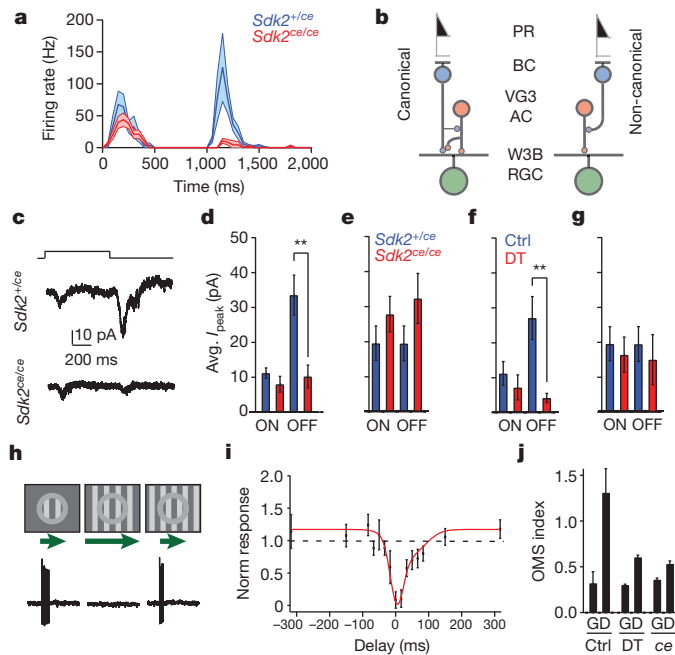


Figure 4 | Excitatory input reaches W3B-RGCs via VG3-ACs. **a**, Average firing rate recorded from W3B-RGCs in *Sdk2^{ce/+}* (blue, $n = 21$) and *Sdk2^{ce/ce}* (red, $n = 10$) retinas in response to a small spot flashed for 1 s. Dark lines, average; shadowing denotes s.e.m. Bin width, 50 ms. **b**, Canonical and non-canonical pathways for delivering OFF input to RGCs. **c**, Excitatory currents recorded from W3B-RGCs in response to a spot flash ($V_h = -65$ mV). **d**, Average peak current (I_{peak}) from experiments such as those shown in **c** ($n = 7$ W3B-RGCs in 4 *Sdk2^{ce/+}* mice and 8 W3B-RGCs in 4 *Sdk2^{ce/ce}* mice; ** $P < 0.01$, Student's *t*-test). **e**, I_{peak} of inhibitory currents recorded from W3B-RGCs in response to a full field flash ($V_h = -5$ mV) ($n = 7$ W3B-RGCs in 5 controls and 5 W3B-RGCs in 4 *Sdk2^{ce/ce}* mice). **f**, I_{peak} of excitatory currents recorded from W3B-RGCs in response to a spot flash ($n = 5$ W3B-RGCs in 3 control mice and 11 W3B-RGCs in 5 *Vglut3-cre;DTR* mice; ** $P < 0.01$, Student's *t*-test). **g**, I_{peak} of inhibitory currents recorded from W3B-RGCs in response to a full field flash ($n = 5$ W3B-RGCs in 5 mice (4 *Sdk2^{ce/+}* mice and 1 control mouse pooled) and 5 diphtheria toxin (DT)-treated *Vglut3-cre;DTR/TYW3* mice). **h**, Object motion stimulus-evoked responses in W3B-RGCs. W3B-RGCs spike vigorously to a grating passed over their receptive field centre (local). They are silenced when the moving grating extends to their surround (global) but not when the centre grating leads or lags that in the surround (differential), as quantified in **i**. **i**, Responses measured in W3B in response to a stimulus where the centre grating began its movement at different times relative to that of the surround. Negative delays are when the centre led the surround. Responses were normalized (Norm) to those evoked by a centre grating alone ($n = 7$ W3B-RGCs). **j**, Responses measured in W3B-RGCs to global (G) and differential (D) motion stimuli normalized to that elicited in control W3B-RGCs with local motion stimuli ($n = 10$ W3B-RGCs in 5 control mice, 6 W3B-RGCs in 4 *Sdk2^{ce/ce}* mice and 9 W3B-RGCs in 3 diphtheria-toxin-treated *Vglut3-cre;DTR/TYW3* mice). OMS, object motion sensitivity. Data in **e–g**, **i** and **j** are mean \pm s.e.m.

delivered to W3-RGCs in an unusual way: while bipolar cells synapse directly on most RGCs³, W3B-RGCs receive OFF input indirectly via VG3-ACs (Fig. 4b). The small, statistically insignificant decrease in the ON response may reflect the presence of other ON inputs that compensate for loss of that normally supplied by VG3-ACs.

Speed is of the essence for visual perception, so it seems odd to interpose an extra synapse between photoreceptors and W3B-RGCs. A clue to the reason for this comes from the fact that W3B-RGCs compare motion in the centre and surround of the receptive field, firing only when the two are asynchronous^{5–7} (Fig. 4h, i). For the comparison to be temporally precise, input from the surround must arrive at the cell rapidly and/or input from the centre must be delayed. Previous studies^{5,7} show that spiking amacrine cells convey rapid inhibition to object-motion-sensing RGCs including W3B-RGCs.

We find that in addition, currents elicited by stimulation of the receptive field centre are delayed in W3B-RGCs relative to other RGCs (Extended Data Fig. 10). We speculate that the interposition of VG3-ACs between bipolar cells and W3B-RGCs contributes to this delay, although it cannot explain it entirely. In addition, VG3-ACs themselves are tuned to differential motion²⁰, presumably accounting for much of the tuned excitatory input that W3B-RGCs receive⁶. Consistent with this interpretation, the ability of W3B-RGCs to distinguish local from global motion is markedly reduced in *Sdk2* mutants or after elimination of VG3-ACs, as evidenced by a reduction in spike rate relative to control for local and differential motion (Fig. 4j) and Extended Data Fig. 10i).

In summary, the recognition molecule *Sdk2* is required for the selective and strong connectivity between *Sdk2*-positive VG3-ACs and W3B-RGCs. Connections of VG3-ACs or W3B-RGCs with proximate but *Sdk2*-negative partners are substantially weaker. Because *Sdk2* is localized at synapses and required in both partners, we speculate that it acts homophilically to promote appropriate connections. In its absence, functional connections fail to form or are not maintained, leading to markedly decreased synaptic strength.

Taken together with previous studies, our data support a multi-step model for synaptic specificity in the IPL. First, one set of recognition molecules, including cadherins and plexins, direct arbors to appropriate sublaminae^{26,27}. Within sublaminae, proximate partners connect at low levels, consistent with Peters' rule^{22–25}. Finally, recognition molecules such as *Sdk* proteins, and perhaps other immunoglobulin superfamily adhesion molecules^{28,29}, act to bias connectivity in favour of specific pairings.

Our results also reveal a role of the VG3-AC-W3B-RGC synapse in visual function. In canonical retinal circuits, bipolar cells relay visual input from photoreceptors to RGCs, whereas amacrine cells, which have been presumed to be inhibitory, modulate this input³ (Fig. 4b). By contrast, VG3-ACs provide the main excitatory drive to the W3B-RGCs. Thus, the VG3-AC-W3B-RGC synapse is a component of a non-canonical retinal circuit in which some of the visual input is relayed to W3B-RGCs through VG3-ACs rather than arriving directly through bipolar cells. This seemingly cumbersome arrangement could improve the sensitivity of W3B-RGCs to the visual features that best excite them—the motion of small objects whose movements are asynchronous with those of the background⁵.

Online Content Methods, along with any additional Extended Data display items and Source Data, are available in the online version of the paper; references unique to these sections appear only in the online paper.

Received 11 October 2014; accepted 22 June 2015.

Published online 19 August 2015.

1. Sanes, J. R. & Zipursky, S. L. Design principles of insect and vertebrate visual systems. *Neuron* **66**, 15–36 (2010).
2. Golisch, T. & Meister, M. Eye smarter than scientists believed: neural computations in circuits of the retina. *Neuron* **65**, 150–164 (2010).
3. Masland, R. H. The neuronal organization of the retina. *Neuron* **76**, 266–280 (2012).
4. Sanes, J. R. & Masland, R. H. The types of retinal ganglion cells: current status and implications for neuronal classification. *Annu. Rev. Neurosci.* **38**, 221–246 (2015).
5. Kim, I. J., Zhang, Y., Meister, M. & Sanes, J. R. Laminar restriction of retinal ganglion cell dendrites and axons: subtype-specific developmental patterns revealed with transgenic markers. *J. Neurosci.* **30**, 1452–1462 (2010).
6. Zhang, Y., Kim, I. J., Sanes, J. R. & Meister, M. The most numerous ganglion cell type of the mouse retina is a selective feature detector. *Proc. Natl. Acad. Sci. USA* **109**, E2391–E2398 (2012).
7. Baccus, S. A., Olveczky, B. P., Manu, M. & Meister, M. A retinal circuit that computes object motion. *J. Neurosci.* **28**, 6807–6817 (2008).
8. Olveczky, B. P., Baccus, S. A. & Meister, M. Segregation of object and background motion in the retina. *Nature* **423**, 401–408 (2003).
9. Venkataramani, S. et al. Distinct roles for inhibition in spatial and temporal tuning of local edge detectors in the rabbit retina. *PLoS ONE* **9**, e88560 (2014).
10. Russell, T. L. & Werblin, F. S. Retinal synaptic pathways underlying the response of the rabbit local edge detector. *J. Neurophysiol.* **103**, 2757–2769 (2010).
11. van Wyk, M., Taylor, W. R. & Vaney, D. I. Local edge detectors: a substrate for fine spatial vision at low temporal frequencies in rabbit retina. *J. Neurosci.* **26**, 13250–13263 (2006).

12. Levick, W. R. Receptive fields and trigger features of ganglion cells in the visual streak of the rabbit's retina. *J. Physiol. (Lond.)* **188**, 285–307 (1967).
13. Yamagata, M., Weiner, J. A. & Sanes, J. R. Sidekicks: synaptic adhesion molecules that promote lamina-specific connectivity in the retina. *Cell* **110**, 649–660 (2002).
14. Yamagata, M. & Sanes, J. R. Dscam and Sidekick proteins direct lamina-specific synaptic connections in vertebrate retina. *Nature* **451**, 465–469 (2008).
15. Yamagata, M. & Sanes, J. R. Synaptic localization and function of Sidekick recognition molecules require MAGI scaffolding proteins. *J. Neurosci.* **30**, 3579–3588 (2010).
16. Haverkamp, S. & Wassle, H. Characterization of an amacrine cell type of the mammalian retina immunoreactive for vesicular glutamate transporter 3. *J. Comp. Neurol.* **468**, 251–263 (2004).
17. Grimes, W. N., Seal, R. P., Oesch, N., Edwards, R. H. & Diamond, J. S. Genetic targeting and physiological features of VGLUT3⁺ amacrine cells. *Vis. Neurosci.* **28**, 381–392 (2011).
18. Johnson, J. et al. Vesicular glutamate transporter 3 expression identifies glutamatergic amacrine cells in the rodent retina. *J. Comp. Neurol.* **477**, 386–398 (2004).
19. Lee, S. et al. An unconventional glutamatergic circuit in the retina formed by VGLUT3 amacrine cells. *Neuron* **84**, 708–715 (2014).
20. Kim, T., Soto F. & Kerschensteiner D. An excitatory amacrine cell detects object motion and provides feature-selective input to ganglion cells in the mouse retina. *eLife* <http://dx.doi.org/10.7554/eLife.08025> (2015).
21. El Mestikawy, S. et al. From glutamate co-release to vesicular synergy: vesicular glutamate transporters. *Nature Rev. Neurosci.* **12**, 204–216 (2011).
22. Peters, A. & Feldman, M. L. The projection of the lateral geniculate nucleus to area 17 of the rat cerebral cortex. I. General description. *J. Neurocytol.* **5**, 63–84 (1976).
23. Stepanyants, A. & Chklovskii, D. B. Neurogeometry and potential synaptic connectivity. *Trends Neurosci.* **28**, 387–394 (2005).
24. Shepherd, G. M., Stepanyants, A., Bureau, I., Chklovskii, D. & Svoboda, K. Geometric and functional organization of cortical circuits. *Nature Neurosci.* **8**, 782–790 (2005).
25. Binzegger, T., Douglas, R. J. & Martin, K. A. A quantitative map of the circuit of cat primary visual cortex. *J. Neurosci.* **24**, 8441–8453 (2004).
26. Duan, X., Krishnaswamy, A., De la Huerta, I., Sanes, J. R. & Type, I. I. Cadherins guide assembly of a direction-selective retinal circuit. *Cell* **158**, 793–807 (2014).
27. Matsuo, R. L. et al. Transmembrane semaphorin signalling controls laminar stratification in the mammalian retina. *Nature* **470**, 259–263 (2011).
28. Yamagata, M. & Sanes, J. R. Expanding the Ig superfamily code for laminar specificity in retina: expression and role of contactins. *J. Neurosci.* **32**, 14402–14414 (2012).
29. Fuerst, P. G., Koizumi, A., Masland, R. H. & Burgess, R. W. Neurite arborization and mosaic spacing in the mouse retina require DSCAM. *Nature* **451**, 470–474 (2008).

Acknowledgements We thank E. Soucy and J. Greenwood for assistance with constructing the two-photon microscope, the Genome Modification Facility at Harvard for generating mouse lines, and E. Feinberg for insight into the ion selectivity of ChR2. This work was supported by grants from the NIH (NS029169 and EY022073) to J.R.S., NSERC (Canada) and Banting Postdoctoral Fellowships to A.K., a HHMI-Life Sciences Research Foundation Postdoctoral Fellowship to X.D., and an NIH fellowship (F31 NS055488) to Y.K.H.

Author Contributions A.K., M.Y. and J.R.S. planned experiments, analysed data and wrote the paper. A.K. performed electrophysiological and histological experiments, M.Y. performed genetic and histological experiments, X.D. developed methods and generated reagents and Y.K.H. generated reagents and performed *in situ* hybridization. The authors declare no competing interest.

Author Information Reprints and permissions information is available at www.nature.com/reprints. The authors declare no competing financial interests. Readers are welcome to comment on the online version of the paper. Correspondence and requests for materials should be addressed to J.R.S. (sanesj@mcb.harvard.edu).

METHODS

Animals. We modified a lambda-phage-mediated recombineering method³⁰ to generate *Sdk1* and *Sdk2* targeting vectors in which the first coding exons of the *Sdk1* and *Sdk2* genes were replaced by an epitope-tagged CreER-T2 recombinase complementary DNA. Tags were three tandem copies of the haemagglutinin (HA) tag (amino acid sequence YPYDVPDYA) for *Sdk1*, and six tandem copies of the Myc tag (amino acid sequence EQKLISEEDL) for *Sdk2*. Loci were modified by homologous combination in V6.5 embryonic stem cells, and chimaeras were produced by the Harvard University Genome Modification Facility. High percentage chimaeras transmitting the knock-in alleles were bred to animals expressing FLP recombinase from the β-actin promoter³¹ to remove the SV40-NEO cassette.

Thy1-STOP-YFP, *TYW3*, *TYW7*, *TYW9*, *Kcnq4-cre* and *Neto1-cre* mice were generated in our laboratory. *Thy1-STOP-YFP* expresses YFP after excision of a stop cassette by Cre recombinase³². *TYW3* mice express YFP in subsets of RGCs⁵. *TYW7* mice express YFP in two types of RGCs, which are present at similar densities; one has its dendrites in the distal half of S3; the other has its dendrites in S1. *TYW9* mice express YFP in ooDSGCs that prefer nasal motion³³. *Neto1-cre* and *Kcnq4-cre* mice express Cre recombinase in type 2 and type 5 bipolar cells, respectively, as well as in subsets of RGCs^{26,34}. *Vglut3-cre* mice were obtained from R. Seals and R. Edwards. In these mice, Cre was inserted into exon 1 of a bacterial artificial chromosome that contained *Vglut3*, and this vector was used to generate a transgenic line¹¹. *Nex-cre* mice, in which Cre is targeted to the endogenous *Neurod6* locus³⁵, were obtained from K. Nave via L. Reichardt; this line expresses Cre in non-GABAergic non-glycinergic (nGnG) and glycinergic SEG amacrine cells³⁶. *DAT-cre* mice, in which Cre is targeted to the endogenous *DAT* (also known as *Slc6a3*) locus, were obtained from X. Zhuang³⁷ via V. Murthy; this line expresses Cre in type II catecholaminergic amacrine cells. *ChAT-cre* mice, in which the Cre recombinase gene was targeted to the endogenous *Chat* gene, was obtained from Jackson Laboratories³⁸; this line expresses Cre in starburst amacrine cells (SACs). Hb9-GFP transgenic mice, which express green fluorescent protein (GFP) in ooDSGCs that prefer nasal motion³⁹, were obtained from K. Eggan. *Rosa-LOX-STOP-LOX-ChR2(H134R)-tdTomato* mice (Ai27), which express channelrhodopsin after excision of a stop cassette by Cre recombinase⁴⁰ were provided by H. Zeng. *Rosa-CAG-LOX-STOP-LOX-DTR* mice, which express DTR following excision of a stop cassette by Cre recombinase, were obtained from Jackson Laboratories⁴¹. The *Rosa-CAGS-LOX-CHERRY-LOX-GFP* line was from S. Dymecki⁴². *Six3-cre* mice⁴³ were provided by W. Klein.

To enable expression of *Sdk2* under Cre-dependent control, we generated a line using a previously described strategy^{44,45}. A cassette encoding Venus and *Sdk2*, separated by tripleF2A (three tandem repeats of foot-and-mouth disease 2A peptide sequence) was cloned into a *Rosa26-CAG-STOP*-targeting vector to generate *Rosa-CAG-LOX-STOP-LOX-Venus-3F2A-Sidekick2-WPRE-FRT-neo-FRT*. Homologous recombinants were selected in the V6.5 embryonic stem cell line and chimaeras were generated. Germ-line chimaeras were crossed to a Flp mouse³¹ to obtain germ-line transmissions and to remove the FRT-neo-FRT sequence.

Animals were used in accordance with NIH guidelines and protocols approved by Institutional Animal Use and Care Committee at Harvard University. Mice were maintained on a C57/B6 background. Both male and female mice were used in this study. Animals were 40 to 100 days old at the time of euthanasia unless otherwise stated in the text or figure legend. Genotypes of mice were known to investigators at the time of the experiment, and there was no randomization in assignment of animals for specific experiments.

RT-PCR. RNA was prepared from the brains of wild-type or knockout mice using EZNA Total RNA kit I (OMEGA bio-tek), reverse-transcribed by SuperScript III (Life Technologies), and amplified using Taq DNA polymerase (EconoTaq PLUS, Lucigen) with these gene-specific PCR primers.

Sdk1 forward: 5'-TGAACCGTCTTCGCAAGGCTACA-3', *Sdk1* reverse: 5'-AAGGGTCAGCTCAGAGCAGATT-3'; *Sdk2* forward: 5'-TTCTGGCTGTAGAAGGCACTCA-3', *Sdk2* reverse: 5'-AGGATGCCGTGATCCTTGCTCA-3'; Cre forward: 5'-GCATTACCGGTCGATGCAACGAGTGATGAG-3', Cre reverse: 5'-GAGTGAACGAACCTGGTCGAAATCAGTGCG-3'; *Gapdh* forward: 5'-TGAAGGTCGGTGTGAACGGATTGTC-3', *Gapdh* reverse: 5'-CATGTAGGCCATGAGGTCCACCAC-3'.

Histology. Mice were euthanized by intraperitoneal injection of pentobarbital and either enucleated immediately or transcardially perfused with Ringer's solution followed by 4% (w/v) paraformaldehyde (PFA) in PBS. Eye cups were removed and fixed in 4% (w/v) PFA in PBS on ice overnight, sunk in 30% (w/v) sucrose/PBS, and mounted in the OCT compound. Immunostaining of cryosections was carried out as described previously^{14,44}. For double immunostaining with two different mouse antibodies, we used the Zenon Horseradish Peroxidase Mouse IgG1 Labelling Kit (Life Technologies) to label one of them, and detected reaction product with TSA-Plus kits (Perkin-Elmer Life Sciences). For immunodetection of epitope-tagged CreER, cryosections were permeabilized in absolute methanol at

−20 °C overnight, treated with Image-iT FX signal enhancer (Life Technologies) as instructed by the manufacturer's protocol, and blocked with 5% (w/v) skim milk (BioRad) in PBS for 30 min at room temperature. The antibodies were diluted in Renoir Red diluent (BioCare Medical), incubated at 4 °C for 48 h, rinsed, and detected with secondary antibodies which had been preabsorbed with acetone powders prepared from mouse brain. In some cases, animals were injected twice with 1 mg tamoxifen (Sigma) in 0.1 ml sunflower oil at 24 and 48 h before culling, resulting in a higher concentration of CreER in the nucleus, which enhanced our ability to detect it.

To label single VG3-ACs and W3B-RGCs, retinae containing dye-filled W3B-RGCs or sparsely labelled VG3-ACs were fixed in 4% PFA at 4 °C for 1 h and then incubated in primary antibodies dissolved in blocking solution (PBS, 0.3% Triton X-100 and 3% donkey serum; Jackson ImmunoResearch) for 7–10 days at 4 °C with agitation. Next, retinae were washed for 3–5 h in 3–5 changes of PBS and incubated with secondary antibodies overnight at 4 °C with agitation. After 3–5 h of washing in PBS with agitation, retinae were flattened onto nitrocellulose membranes (Millipore) and mounted on slides (Vectashield, Vector Labs).

To generate antibodies to mouse *Sdk1* and *Sdk2*, ~100 amino-acid-long stretches of the intracellular domains were selected in a region where the two molecules maximally differ in amino acid sequence. cDNAs encoding these fragments fused to a poly-histidine tag were inserted into a pET vector (Novagen). Fusion proteins were produced in BL21 bacteria and purified using a His-column (Life Technologies). Animals were immunized and antisera produced by Covance Research. Antibodies were affinity purified using the antigen fusion proteins as bait. We also generated mouse polyclonal antibodies to mouse *Sdk1* and *Sdk2* by immunizing *Sdk1*- and *Sdk2*-knockout mice with L cells (ATCC) that had been transfected with full-length mouse *Sdk1* or *Sdk2* cDNA as described previously²⁸. Antibodies were tested on *Sdk1*- and *Sdk2*-expressing HEK cells (HEK-293T; ATCC) and on retinal tissue from *Sdk1*^{cre/cre} and *Sdk2*^{cre/cre} mice to verify specificity.

Antibodies used in this study were: rabbit monoclonal antibody to oestrogen receptor alpha (Clone SP1, from Epitomics or Abcam); goat anti-Myc (NB600-335, from Novus); rat anti-HA (3F10, from Roche Diagnostics); anti-Brn3a (clone, 5A3.2), rabbit anti-synapsin I (AB1543P), mouse anti-calretinin (clone, 6B8.2), goat anti-ChAT antibodies, and sheep anti-tyrosine hydroxylase from Millipore; AP2 (clone, 3B5), SV2, anti-synaptotagmin 2 (clone, ZN1P) from Developmental Studies Hybridoma Bank; mouse anti-VGluT1 (clone, N28/9), mouse anti-pan-MAGUK (clone, N28/86), mouse anti-HCN4 (clone, N114.10), and mouse anti-Vesicular acetylcholine transporter (clone, N6/38) from NeuroMab; mouse anti-SATB2 (clone, 4B19) from Abcam; rabbit anti-fluorescein (Life Technologies); and rabbit anti-protein kinase C alpha (P4334) from Sigma. Rabbit antibody to Dab1 was a gift from B. Howell. Rabbit anti-lucifer yellow and anti-fluorescein were from Invitrogen. Chicken anti-GFP and rabbit anti-mCherry were generated as described previously^{42,44}. Nuclei were labelled with NeuroTrace Nissl 435 (Life Technologies). Secondary antibodies were conjugated to DyLight 488, DyLight 594, or Alexa 647 (Jackson ImmunoResearch).

For *in situ* hybridization, riboprobes were synthesized from *Sdk1* or *Sdk2* cDNAs using digoxigenin- or fluorescein-labelled UTP and hydrolysed to around 500 base pairs as described previously^{13,15}. Probes were detected using anti-digoxigenin antibodies conjugated to alkaline phosphatase, followed by reaction with BCIP (5-bromo-4-chloro-3-indolyl phosphate) and NBT (nitroblue tretrazolium) substrate for 24–36 h; or using anti-digoxigenin and anti-fluorescein antibodies conjugated to horseradish peroxidase, followed by amplification with tyramide conjugates (TSA-Plus system; Perkin-Elmer Life Sciences).

Imaging. Images of immunostained retinal wholemounts were acquired on a LSM 710 confocal microscope using a 63× water immersion objective. Images were acquired at a resolution of 1,024 × 1,024 pixels with a step size of 0.2–0.5 mm. ImageJ was used to generate maximum intensity projections of singly labelled neurons and skeletonized dendrites in the x-y and x-z planes.

Image stacks were registered using stackreg (ImageJ). Images of single VG3-ACs and W3B-RGCs taken from P30-40 retinae were skeletonized manually through the z-stack using simple neurite tracer (ImageJ). Path ROIs describing neuronal processes were converted to line stacks and used for morphological analysis using the Trees toolbox⁴⁶. We measured the projection depth of VG3-ACs and W3B-RGCs by taking the z-axis intensity profile of labelled neurons and plotted this profile as a percentage of IPL depth. IPL depth in turn was defined by ChAT-counterstained somas that label SACs in the GCL and IPL. The investigators were not blinded to allocation during image analysis.

Channelrhodopsin excitation. ChR2-tdTomato-positive interneurons were first imaged at low power (2–4 mW sample plane power at 960 nm) and a stack of their cell body positions was acquired. Somata were highlighted as regions of interest (ROIs) until all available interneurons were marked within the stack (typically 250 × 200 × 4 μm). Custom software written in LabView (National Instruments) used these ROIs to steer the beam to soma locations and activate ChR2 using either

raster or spiral scan trajectories ($\sim 25\text{--}30\text{ mW}$ sample plane power at 920 nm). Dwell times in these scan patterns were $0.02\text{--}0.05\text{ ms pixel}^{-1}$, which was less than the rise time of the current produced by a stationary spot (Extended Data Fig. 3c, g–j). Pixel size was $0.6\text{ }\mu\text{m}^2$ and scan patterns typically contained 100 pixels with their total time synchronized to the laser shutter, which opened for 2 ms.

We arrived at these parameters by measuring the kinetics of ChR2 responses on HEK cells and retinal neurons that expressed ChR2(H134R) (Extended Data Fig. 3). Our goal was to scan interneuron somas (typically 10×10 pixels in size) and activate them with a current step that would imitate the square current pulses used when stimulating interneurons via a sharp electrode⁴⁷. Responses in ChR2-expressing HEK cells elicited by a stationary spot of infrared laser light at a range of wavelengths between 800 and 960 nm (840 nm, 860 nm and 920 nm are shown in Extended Data Fig. 3b, c) led us to conclude that 920 nm would be a good compromise between response size, rise time and sample plane power. Currents typically had $<2\text{ ms}$ rise times (10–90%) with peak amplitudes of $150\text{--}175\text{ pA}$ at 25 mW sample plane power (Extended Data Fig. 3a). Increasing stimulus duration beyond $2\text{--}3\text{ ms}$ produced no increase in peak amplitude and instead the response showed signs of desensitization^{48–51} (Extended Data Fig. 3a). Taken together, these results would suggest that responses evoked by 920 nm light would saturate at dwell times greater than 2 ms pixel^{-1} .

Next, we measured the spatial dimension of two-photon laser stimulation of ChR2. To do this, we recorded from ChR2 expressing HEK cells while stimulating the HEK cell at different positions away from the edge of the cell membrane (Extended Data Fig. 3d), or while stimulating the HEK cell at different heights beginning at the cell membrane (Extended Data Fig. 3f). Taken together, these results indicate that two-photon laser stimulation of ChR2 has maximal $x\text{-}y\text{-}z$ dimensions of approximately $3 \times 3 \times 5\text{ }\mu\text{m}$. Next, we recorded from ChR2-positive RGCs or SACs, highlighted their somas with ROIs and steered the beam through these ROIs in raster or spiral scan trajectories at different dwell times to produce currents of $250\text{--}350\text{ pA}$ with $<2\text{ ms}$ rise times (Extended Data Fig. 3g–j). Empirically, this dwell time tended to be $0.02\text{--}0.05\text{ ms pixel}^{-1}$. Currents were similar at both dwell times. Finally, we determined the relationship between inward currents on W3B to stimulation of VG3-ACs at different sample plane powers. This experiment revealed a classical sigmoid relationship between the size of the postsynaptic response and the strength of the stimulus (power at the sample plane) delivered to VG3-ACs consistent with calcium dependence of transmitter release⁵² (Extended Data Fig. 3l). Sample plane powers used in our analysis of connectivity ($25\text{--}30\text{ mW}$) sit on the plateau of this curve and are 4–6 times the power levels that evoke a minimal response. We observed signs of infrared-light induced damage on cultured cells as well as retinal tissue at sample plane powers greater than 40 mW .

Under the conditions we used, photoreceptor-evoked light responses on RGCs were rarely seen. To confirm this independence, we activated ChR2 and photoreceptors independently and observed distinctly different kinetics²⁶ (Extended Data Fig. 4g). These data establish that our functional connectivity measurements are not contaminated by light responses. Nevertheless, we avoided exposure times of $>100\text{ ms}$ owing to a well described relationship between exposure time and infrared-evoked light responses⁵². Even in these cases, however, ChR2-positive interneuron-evoked responses were clearly distinguishable from light responses owing to the marked differences in their latencies ($>50\text{ ms}$ for light responses).

For experiments in which we activated ChR2 with blue light, we incubated the retina in a cocktail of blockers as described previously¹⁹. (10 mM ACET ((S)-1-(2-amino-2-carboxyethyl)-3-(2-carboxy-5-phenylthiophene-3-yl-methyl)-5-methylpyrimidine-2,4-dione)⁵³, Tocris; 20 mM L-AP4 (L-(+)-2-amino-4-phosphonobutyric acid), Tocris; $300\text{ mM hexamethonium}$, Sigma). To activate ChR2, we focused light from a 500 mW 470 nm LED (Thor Labs) onto the retina using a relay lens and a $5\times$ objective. LED activation was synchronized to the recordings similar to above for two-photon recordings.

Electrophysiology. Mice were dark-adapted for at least 2 h before euthanasia. The retina was rapidly dissected under infrared illumination into oxygenated ($95\% \text{ O}_2$; $5\% \text{ CO}_2$) Ames solution (Sigma), then placed in a recording chamber with RGCs facing up. Labelled neurons were imaged under two-photon illumination and targeted for recording. For cell-attached recordings, the patch electrodes ($4\text{--}7\text{ M}\Omega$) were filled with Ames solution. For whole-cell recordings, the electrodes were filled with an internal solution containing 120 mM K-acetate , 10 mM Na-acetate , 0.2 mM CaCl_2 , 1 mM MgCl_2 , 10 mM EGTA , 2 mM NaATP , 0.3 mM MgGTP , 5 mM KCl and 10 mM HEPES . Fluorescein 3,000 MW dextran (Invitrogen) was also added to the internal solution to make the electrode visible under two-photon illumination. The chloride reversal potential under these conditions is $\sim -70\text{ mV}$, allowing good separation of inhibitory and excitatory currents in whole-cell mode. For excitatory currents, $V_h \approx -70\text{ mV}$ (E_{Cl}), and for inhibitory currents, $V_h \approx -10\text{ mV}$ ($E_{\text{glutamate}}$); these values were determined for each cell with a voltage ramp stimulus. Only cells with a V_m value more negative

than -50 mV and series resistances of less than $25\text{ M}\Omega$ were used. $40\text{ }\mu\text{M}$ 2,3-dioxo-6-nitro-1,2,3,4-tetrahydrobenzo[f] quinoxaline-7-sulfonamide (NBQX, Tocris), $100\text{ }\mu\text{M}$ picrotoxin (Tocris), $3\text{ }\mu\text{M}$ strichnine (Tocris) and CdCl_2 (Sigma) were dissolved in Ames. After recording, retinas were processed for histology (see above) and immunostained with antibodies against fluorescein to visualize RGC morphologies.

Signals from loose-patch and whole-cell recordings were acquired with a MultiClamp 700B amplifier (Molecular Devices) and with custom software written in LabView. For spikes, Multiclamp was put into $I = 0$ mode and signals were high pass filtered at 1 Hz. For currents, signals were digitized at 20 kHz. An unfiltered output of membrane current was taken in parallel to monitor recording quality. Series resistance for all recordings was not compensated.

Currents were processed by custom software written in Matlab (Simulink) and were analysed as follows: First, currents averaged from ~ 10 stimulus repetitions were split into those that evoked currents (connected) and those that did not (disconnected) in a partially automated way using the following criteria: (1) averaged traces had to have peak currents that were one standard deviation above the pre-stimulus average baseline; and (2) the variance about the mean current had to be $<15\%$ to confirm that stimulus locked currents were present in each individual trial. Once categorization was complete, traces were analysed for their rise times, decay times, onset latency, and sizes. These measurements were then remapped to the stimulated position of the interneuron. Graphs of these processed values were plotted in Igor Pro (WaveMetrics), saved as image files and inserted into figure layouts using Adobe Illustrator. A similar classification procedure was used for analysis of light evoked currents. Data from $Sdk2^{e/+}$ and $Sdk2^{+/+}$ mice were pooled for analysis.

Visual stimuli. Visual stimuli were delivered via a projector as described²⁶. In brief, all visual stimuli were written in Matlab using the psychophysics toolbox and displayed on the projector with a background intensity set to $1 \times 10^4 R^* \text{ rod}^{-1} \text{ s}^{-1}$, in which R^* denotes activated rhodopsin.

The ON receptive field is larger than the OFF receptive field in W3B-RGCs⁶ and slightly off-centre spots can bias the relative sizes of ON and OFF inward currents. To ensure that this innate feature of W3B-RGCs did not influence our measurements of ON and OFF current sizes, we delivered white noise stimuli to W3B-RGCs while recording inward currents. Next, we reverse correlated these currents to the stimuli and created an average that described the receptive field centre. These receptive fields were used as stimuli to measure the sizes of ON and OFF inward currents. Currents in wild-type animals had a canonical shape and showed that the peak OFF current is typically 4–8 times larger than ON current (Fig. 4).

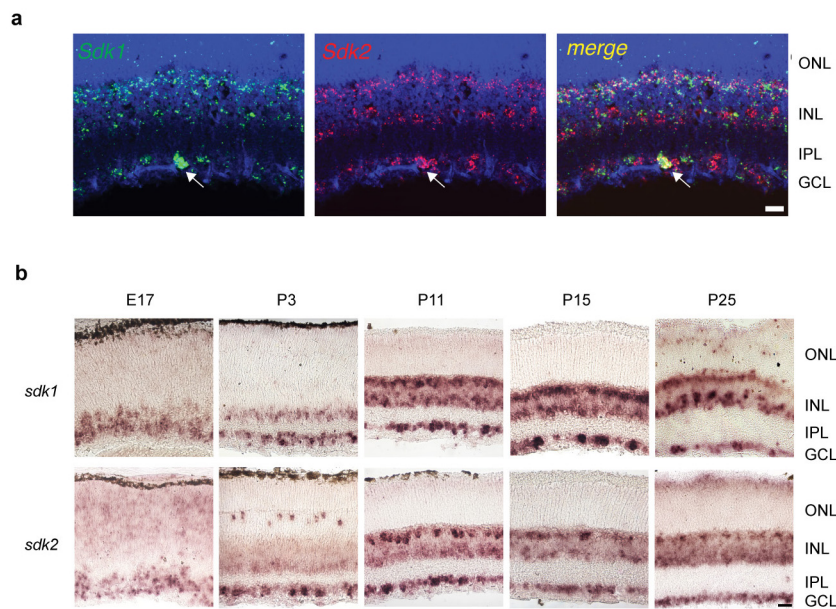
For our differential motion stimulus, we first mapped the W3B-RGCs receptive field using a grid of flashing spots and measured spikes in $I = 0$ mode. Next, we centred a circular object region ($100\text{--}150\text{ }\mu\text{m}$) over the receptive field, bounded it with a grey annulus ($50\text{--}70\text{ }\mu\text{m}$) and created a background region that extended from the annulus to edge of our projected image. Differential motion stimuli were constructed as previously reported^{6,8} and consisted of bars of $40\text{--}72\text{ }\mu\text{m}$ in width that alternated in intensity about our adapting grey level and moved at a speed of $100\text{ }\mu\text{m s}^{-1}$, for a single bar width. For local motion, bars were passed within the object region while the background was set to grey. For global motion, bars were passed over the object and background regions. For differential motion, we passed bars over the full field but moved them in the object region at the following times before or after bars movement in the background: 333.33 ms , 166.67 ms , 100 ms , 83.3 ms , 66.67 ms , 50 ms , 33.33 ms , 16.67 ms , 0 ms (Fig. 4i). These correspond to a difference of 20 , 10 , 5 , 4 , 3 , 2 , 1 and 0 frames of our 60-Hz projector. Responses at these different timings were collected and normalized to the response obtained under local motion only. W3B-RGCs are strongly silenced by activation of their surround, and as a result do not fire when bar movement in the two regions were synchronous. The OMS index (Fig. 4j) was computed by normalizing the average firing rate in response to differential and global motion to that measured in response to local motion. Average firing rates used for this procedure are shown in Extended Data Fig. 10i.

Diphtheria toxin injection. Diphtheria toxin (Sigma) was first dissolved in PBS at 1 mg ml^{-1} and then aliquoted at $-80\text{ }^\circ\text{C}$. Freshly thawed diphtheria toxin aliquot was diluted in PBS and delivered as intraperitoneal injection at $1\text{ }\mu\text{g per 50 g body weight}$ ⁴¹ to 7–10-week-old *Vglut3-cre*; *Rosa-LOX-STOP-LOX-DTR*; TWY3 mice. The dose was repeated four times at 2-day interval. As controls, we injected diphtheria toxin in control animals and saline in *Vglut3-cre*; *Rosa-LOX-STOP-LOX-DTR*; TWY3 animals.

AAV-mediated gene transfer. Viral-mediated gene transfer was performed as described²⁶. For initial connectivity measurements, adeno-associated virus (AAV)-expressing Cre-dependent ChR2-YFP (rAAV2/9-hEF1a-DIO-ChR2 (H134R)-YFP-WPRE, AV-9-20297P, Penn Vector Core) was at a titre of $\sim 1 \times 10^{13}$ genome copies per ml, as described previously²⁶. All of these initial viral experiments were repeated using the Ai27 line. Similar results were obtained with both methods, and results from both methods were pooled.

Statistical methods. No statistical method was used to predetermine sample size. Data sets were tested for normality and statistical differences were examined using the Student's *t*-test (Igor Pro). Variance in the estimate of the mean is shown as s.e.m.

30. Chan, W. *et al.* A recombineering based approach for high-throughput conditional knockout targeting vector construction. *Nucleic Acids Res.* **35**, e64 (2007).
31. Rodríguez, C. I. *et al.* High-efficiency deleter mice show that FLPe is an alternative to Cre-loxP. *Nature Genet.* **25**, 139–140 (2000).
32. Buffelli, M. *et al.* Genetic evidence that relative synaptic efficacy biases the outcome of synaptic competition. *Nature* **424**, 430–434 (2003).
33. Kay, J. N. *et al.* Retinal ganglion cells with distinct directional preferences differ in molecular identity, structure, and central projections. *J. Neurosci.* **31**, 7753–7762 (2011).
34. Duan, X. *et al.* Subtype-specific regeneration of retinal ganglion cells following axotomy: effects of osteopontin and mTOR signaling. *Neuron* **85**, 1244–1256 (2015).
35. Goebels, S. *et al.* Cre/loxP-mediated inactivation of the bHLH transcription factor gene NeuroD/BETA2. *Genesis* **42**, 247–252 (2005).
36. Kay, J. N., Voinescu, P. E., Chu, M. W. & Sanes, J. R. Neurod6 expression defines new retinal amacrine cell subtypes and regulates their fate. *Nature Neurosci.* **14**, 965–972 (2011).
37. Zhuang, X., Masson, J., Gingrich, J. A., Rayport, S. & Hen, R. Targeted gene expression in dopamine and serotonin neurons of the mouse brain. *J. Neurosci. Methods* **143**, 27–32 (2005).
38. Rossi, J. *et al.* Melanocortin-4 receptors expressed by cholinergic neurons regulate energy balance and glucose homeostasis. *Cell Metab.* **13**, 195–204 (2011).
39. Trenholm, S., Johnson, K., Li, X., Smith, R. G. & Awatramani, G. B. Parallel mechanisms encode direction in the retina. *Neuron* **71**, 683–694 (2011).
40. Madisen, L. *et al.* A toolbox of Cre-dependent optogenetic transgenic mice for light-induced activation and silencing. *Nature Neurosci.* **15**, 793–802 (2012).
41. Buch, T. *et al.* A Cre-inducible diphtheria toxin receptor mediates cell lineage ablation after toxin administration. *Nature Methods* **2**, 419–426 (2005).
42. Dymecki, S. M., Ray, R. S. & Kim, J. C. Mapping cell fate and function using recombinase-based intersectional strategies. *Methods Enzymol.* **477**, 183–213 (2010).
43. Furuta, Y., Lagutin, O., Hogan, B. L. & Oliver, G. C. Retina- and ventral forebrain-specific Cre recombinase activity in transgenic mice. *Genesis* **26**, 130–132 (2000).
44. Yamagata, M. & Sanes, J. R. Transgenic strategy for identifying synaptic connections in mice by fluorescence complementation (GRASP). *Front. Mol. Neurosci.* **5**, 18 (2012).
45. Lefebvre, J. L., Kostadinov, D., Chen, W. V., Maniatis, T. & Sanes, J. R. Protocadherins mediate dendritic self-avoidance in the mammalian nervous system. *Nature* **488**, 517–521 (2012).
46. Cuntz, H., Forstner, F., Borst, A. & Häusser, M. One rule to grow them all: a general theory of neuronal branching and its practical application. *PLOS Comput. Biol.* **6**, e1000877 (2010).
47. Asari, H. & Meister, M. The projective field of retinal bipolar cells and its modulation by visual context. *Neuron* **81**, 641–652 (2014).
48. Rickgauer, J. P. & Tank, D. W. Two-photon excitation of channelrhodopsin-2 at saturation. *Proc. Natl. Acad. Sci. USA* **106**, 15025–15030 (2009).
49. Prakash, R. *et al.* Two-photon optogenetic toolbox for fast inhibition, excitation and bistable modulation. *Nature Methods* **9**, 1171–1179 (2012).
50. Andrasfalvy, B. K., Zemelman, B. V., Tang, J. & Vaziri, A. Two-photon single-cell optogenetic control of neuronal activity by sculpted light. *Proc. Natl. Acad. Sci. USA* **107**, 11981–11986 (2010).
51. Katz, B. & Miledi, R. The release of acetylcholine from nerve endings by graded electric pulses. *Proc. R. Soc. Lond.* **167**, 23–38 (1967).
52. Euler, T. *et al.* Eye cup scope-optical recordings of light stimulus-evoked fluorescence signals in the retina. *Pflügers Arch.* **457**, 1393–1414 (2009).
53. Borghuis, B. G., Looger, L. L., Tomita, S. & Demb, J. B. Kainate receptors mediate signaling in both transient and sustained OFF bipolar cell pathways in mouse retina. *J. Neurosci.* **34**, 6128–6139 (2014).

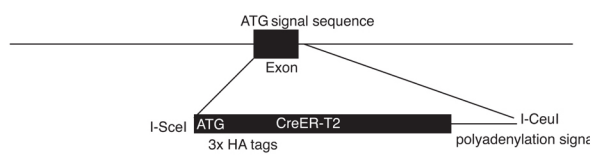

Extended Data Figure 1 | Expression of *Sdk1* and *Sdk2* in developing retina.

a, Double-label *in situ* hybridization for *Sdk1* and *Sdk2* at P10. Arrow indicates a retinal ganglion cell that expresses both *Sdk* genes. Label in INL includes

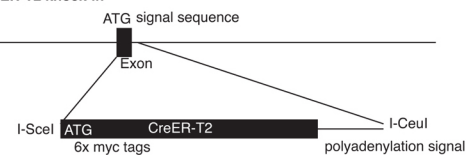
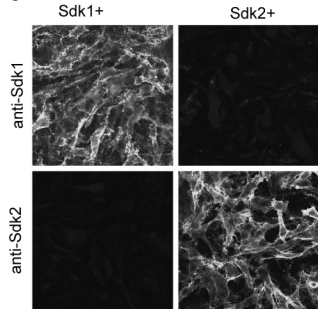
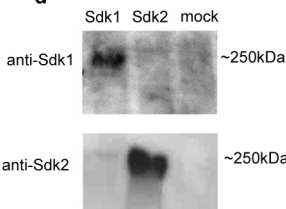
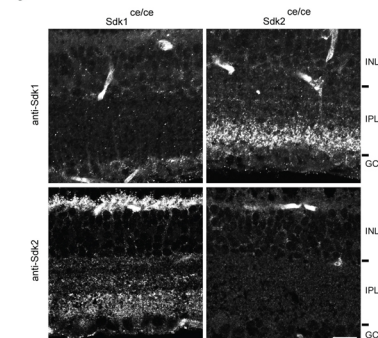
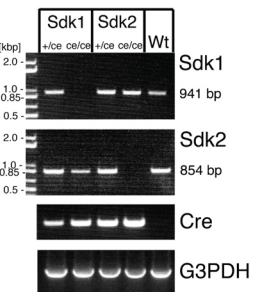
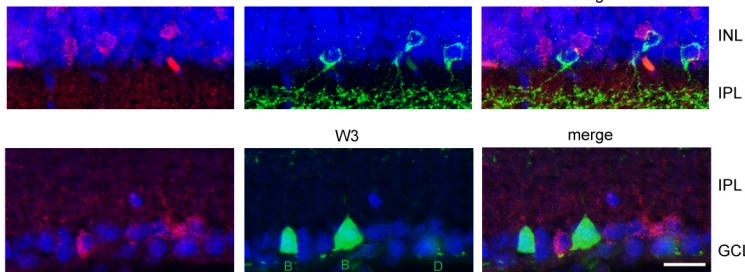
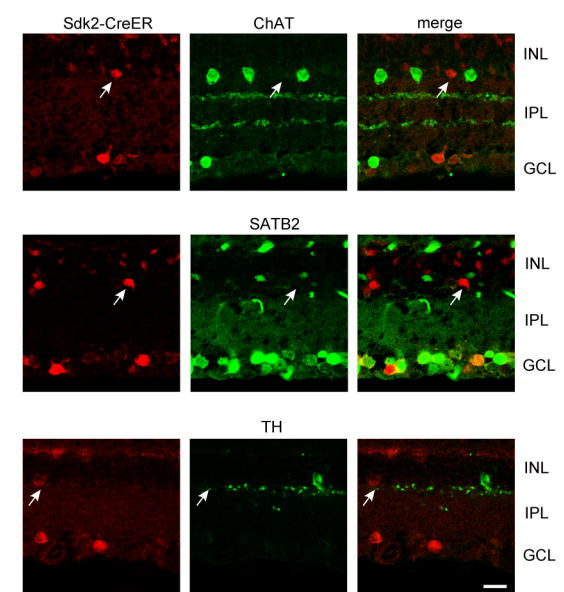
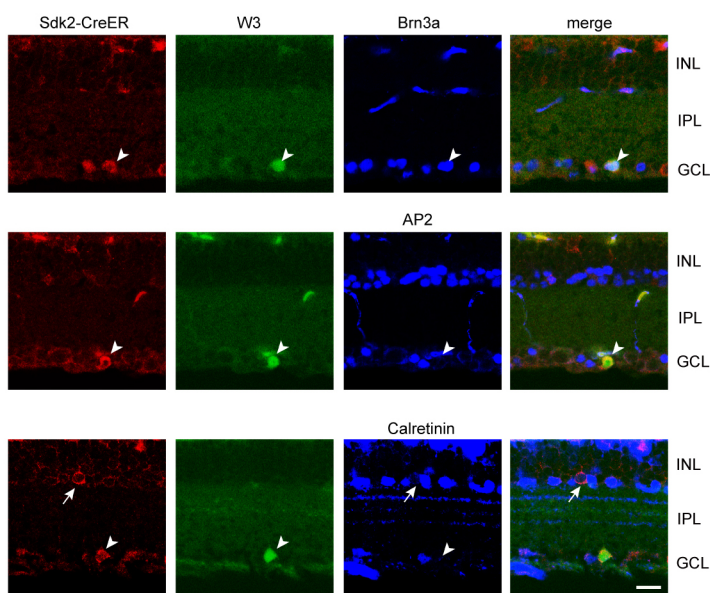
amacrine and bipolar cells, as summarized in Fig. 1k. Other images (not shown) reveal that *Sdk2* is also expressed by horizontal cells. **b**, *In situ* hybridization for *Sdk1* and *Sdk2* RNA at indicated postnatal ages. Scale bars, 10 μ m.

a

Sdk1 Knock-out/CreER-T2 knock-in

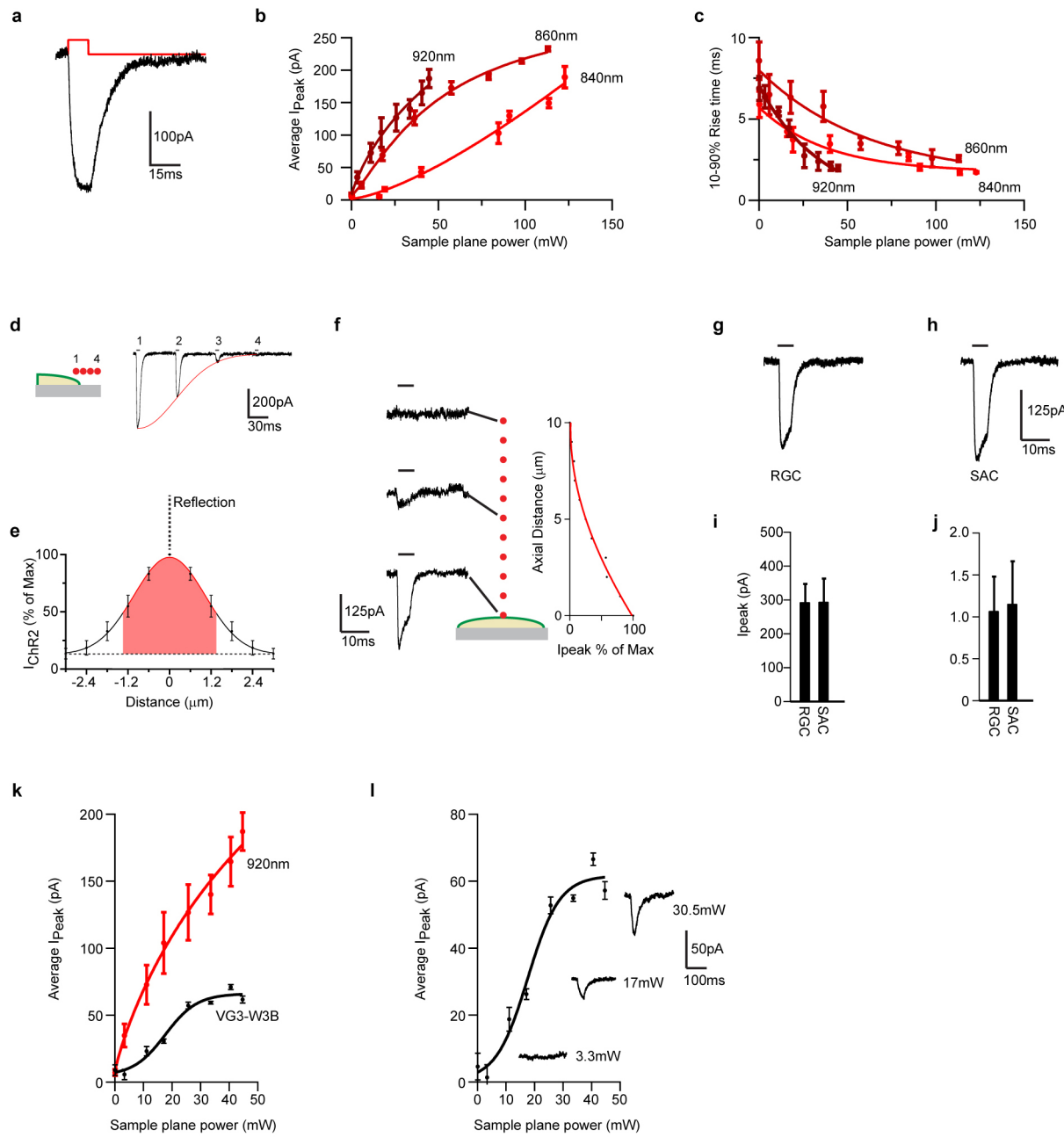
**b**

Sdk2 Knock-out/CreER-T2 knock-in

**c HEK293 cells****d****e****f****g Sdk1-CreER****i****h**

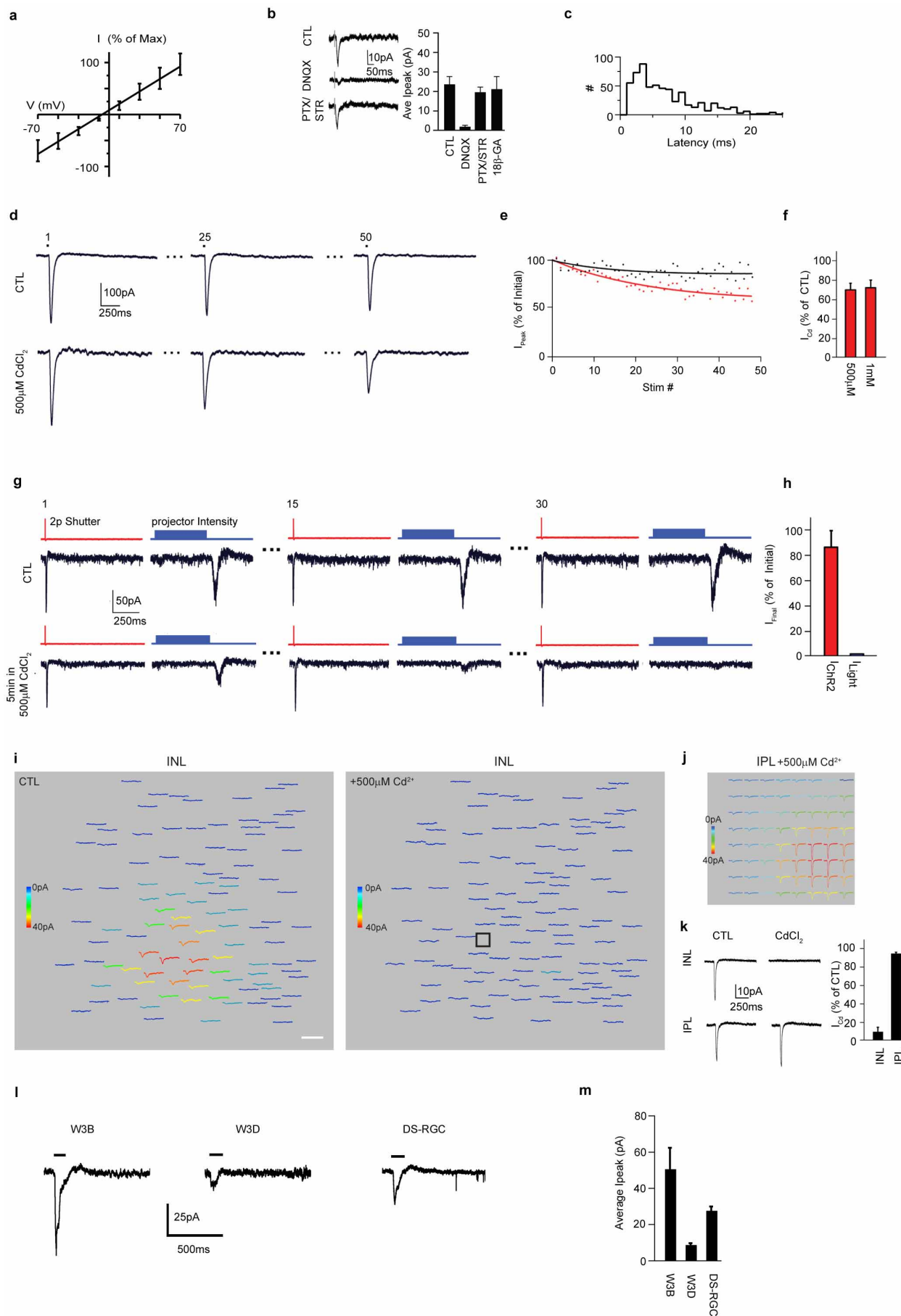
Extended Data Figure 2 | Generation and characterization of *Sdk1* and *Sdk2* knock-in mice **a, b**, Targeting vectors used to generate *Sdk1^{ce/ce}* (**a**) and *Sdk2^{ce/ce}* (**b**) mice. **c**, HEK293 cells transfected with expression vectors encoding *Sdk1* or *Sdk2*, followed by staining with mouse antibodies to *Sdk1* and *Sdk2*. **d**, HEK293 cells transfected with expression vectors encoding *Sdk1* or *Sdk2*, followed by immunoblotting with rabbit polyclonal antibodies to *Sdk1* and a mouse monoclonal antibody to *Sdk2* (CS22). **e**, Retinal sections from P30 *Sdk1^{ce/ce}* and *Sdk2^{ce/ce}* mice stained with mouse antibodies to *Sdk1* and *Sdk2*. Signal on blood vessels is nonspecific. **f**, Reverse transcription PCR (RT-PCR) from *Sdk1^{ce/+}*, *Sdk1^{ce/ce}*, *Sdk2^{ce/+}*, *Sdk2^{ce/ce}* and wild-type (WT) mice. Total RNA was prepared from brain. G3PDH, glyceraldehyde-3-phosphate

dehydrogenase. **g**, VG3-ACs and W3B-RGCs are *Sdk1*-negative. CreER expressed in P30 *Sdk1^{ce/+}* mouse was stained with antibodies to the oestrogen receptor and vesicular glutamate transporter 3 (VG3). Bottom row shows CreER and YFP double staining in a *Sdk1^{ce/+}*; TYW3 mouse. **h**, *Sdk2*-expressing W3B cells express the RGC marker Brn3a, but not the amacrine cell marker AP2. Calretinin is expressed in all the SACs, a subpopulation of type II catecholaminergic cells (CAII) amacrine cells and some RGCs. **i**, SACs (ChAT-positive), type I catecholaminergic (tyrosine hydroxylase-positive), SEG (glycinergic) and nGnG (Satb2-positive³⁵), amacrine cells do not express *Sdk2*. Scale bars, 10 μm.



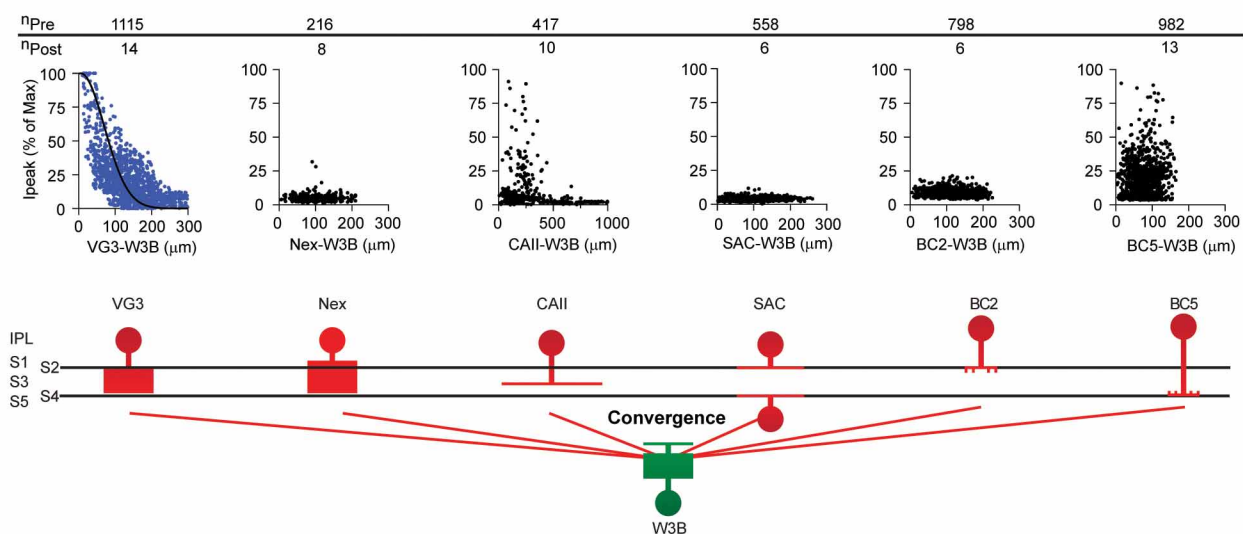
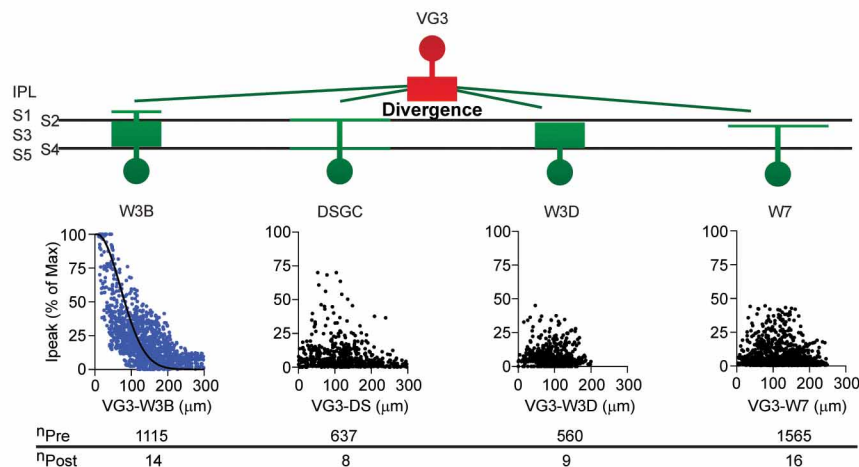
Extended Data Figure 3 | Optimization of optogenetic methods. **a**, Sample current recorded from a ChR2-YFP-expressing HEK cell in response to a stationary PSF-sized spot of 920-nm laser stimulation for 7 ms. **b**, Plot of average peak current measured on ChR2-YFP-expressing HEK cells in response to a stationary point spread function (PSF)-sized spot of laser stimulation at 840 nm, 860 nm and 920 nm for a range of different powers. The 920 nm light produced the largest currents for the least power. **c**, Plot of the rise time (10–90%) of currents to a stationary, PSF-sized spot of laser stimulation at 840 nm, 860 nm and 920 nm for a range of different powers. The 920 nm light produced the shortest rise time for the least power. **d**, Cartoon of a HEK cell with four adjacent PSF-sized spots that start on the edge of the cell and extend off (left). Sample currents evoked by stimulation of these regions. Currents decrease in size as the PSF moves away from the cell. **e**, Quantification of the experiment illustrated in **d** for 5 cells. The curve was obtained in only one direction and reflected about the y axis to give a measure of the x-y spread of ChR2 excitation. **f**, Cartoon of a HEK cell stimulated by a stationary, PSF-sized spot at 10 adjacent 1- μ m planes that extend from the cell surface to $-10\ \mu$ m. Sample currents evoked by this procedure at the indicated z-positions. Average peak current measured on four cells for this procedure

(right) show the z-extent of ChR2 excitation. **g**, Sample current evoked in a ChR2-expressing RGC in response to stimulating an ROI (10×15) with a dwell time of 0.03 ms, taking a total time of 5 ms. **h**, Sample current evoked in a ChR2-expressing SAC in response to stimulating an ROI (10×15) with a dwell time of 0.03 ms, taking a total time of 5 ms. **i**, Average peak current evoked in RGCs and SACs in response to the stimuli shown in **g** and **h** ($n = 6$ cells). **j**, Average rise time (10–90%) of currents evoked on RGCs and SACs in response to the stimuli shown in **g** and **h** ($n = 6$ cells). **k**, Plot of average peak current measured in a W3B-RGC in response to stimulation of VG3-ACs with two-photon stimulation (920 nm) for a range of sample plane powers. Average current size shows a sigmoid relationship. Responses plateau at 25 mW sample plane power ($n = 6$ W3B-VG3 pairs in two animals). I_{peak} versus power relationship from **b** has been re-plotted for comparison. **l**, I_{peak} versus sample plane power measured on W3B-RGCs to VG3-AC replotted from **k**. Sample currents beside the curve were evoked by the powers indicated. Responses require a threshold amount of excitation in VG3-ACs; probably owing to calcium-dependent vesicle release mechanisms ($n = 6$ W3B-VG3 pairs in two animals).



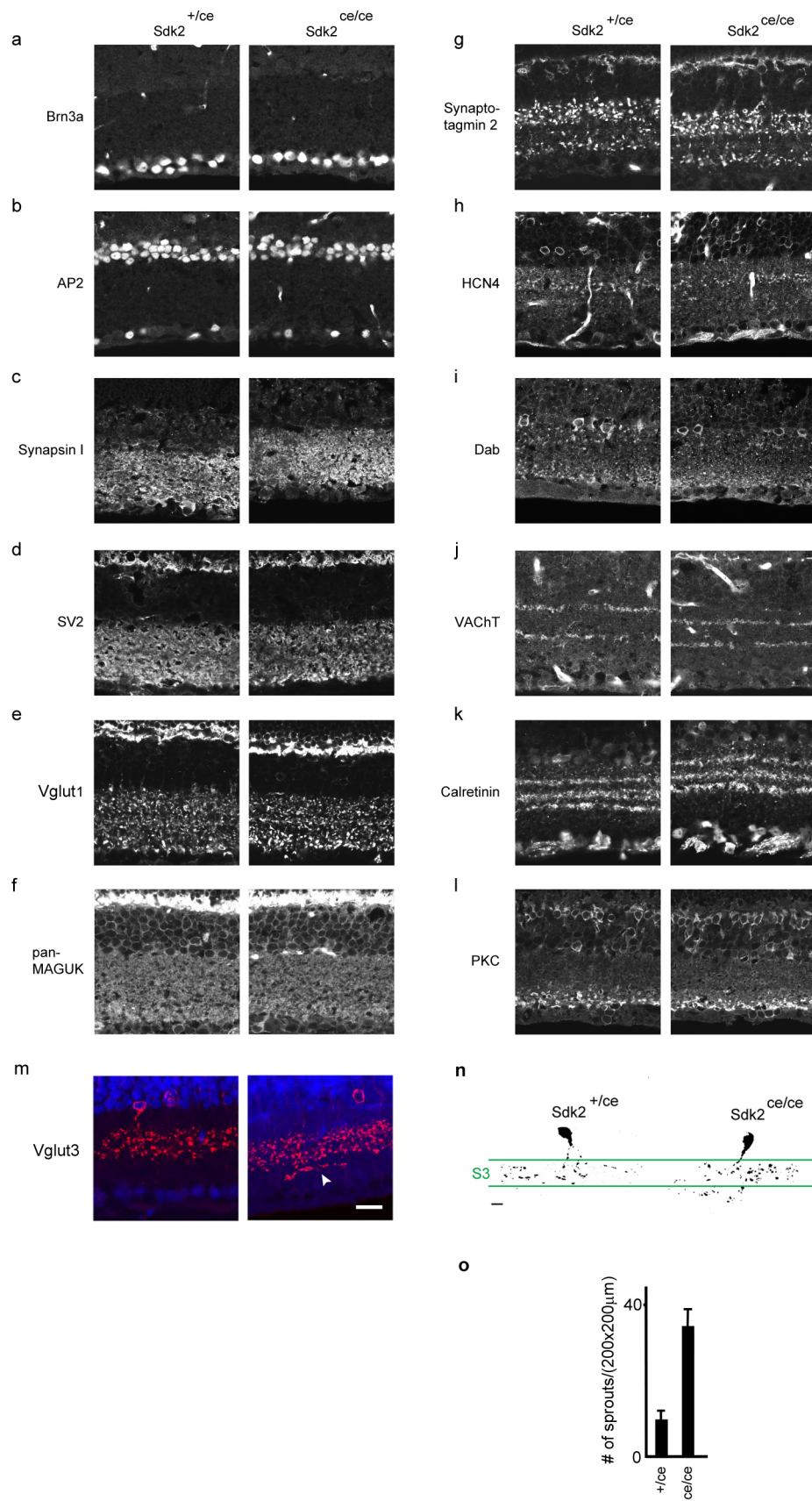
Extended Data Figure 4 | VG3-ACs form direct excitatory synapses on W3B-RGCs. **a**, Average current (I)–voltage (V) plot of VG3-AC evoked currents on W3B-RGCs. Currents were normalized to the maximum inward current per cell ($n = 10$ VG3-W3B pairs). **b**, Currents are abolished by inhibitors of AMPA-type glutamate receptors (DNQX, 20 μM), but are unaffected by inhibitors of GABA (picrotoxin (PTX), 100 μM), glycine (strychnine (STR), 3 μM) receptors and gap junctions (18 β -glycyrhetic acid (18 β -GA), 25 μM) ($n = 8$ –10 per condition). **c**, Latency of VG3-AC-evoked currents on W3B ($n = 623$ VG3s and 14 RGCs). **d**, Inward currents measured in HEK cells transiently transfected with constructs containing ChR2-GFP. The first, twenty-fifth and fiftieth responses to a train (1 Hz) of 60 stimuli are shown for HEK cells recorded in control and CdCl₂-containing solution. **e**, Peak currents from the experiment shown in **a**, plotted as a percentage of the initial peak size. Currents in CdCl₂ appear to decrease slightly over time. **f**, Quantification of peak currents measured in Cd²⁺-containing solution expressed as a percentage of those found in control solution. ChR2 activity is largely unaffected by the presence of CdCl₂ ($n = 6$ cells, in control solution, 10 cells in 500 μM and 8 cells in 1 mM CdCl₂ solution). **g**, Responses of a ChR2-positive RGC to stimulus train that alternated between two-photon excitation of ChR2 on the RGC soma and one-photon activation of photoreceptors above the RGC. The first, fifteenth and thirtieth responses in the train are shown. ChR2 responses are insensitive to the calcium channel blocker but light responses are not. **h**, Peak current measured on the final pulse of the train expressed as a percent of the first for the experiments performed like that in **e**. I_{ChR2} is largely immune to the calcium channel blocker CdCl₂ ($n = 4$ ChR2-positive RGCs). **i**, Heat map of VG3-AC responses measured in a W3B-RGC in control solution (left) and the same heat map measured in the presence of 500 μM CdCl₂. VG3-AC responses initiated by soma stimulation require functional voltage gated calcium channels in the nerve terminals. **j**, Heat map of VG3-AC responses measured in the same W3B-RGC in CdCl₂ solution shown

in **f** in response to a 10 \times 10 stimulus grid (grid square = 5 \times 5 pixels) in the inner plexiform layer. Activating ChR2 on VG3-AC nerve terminals produces responses in W3B-RGCs in spite of silencing voltage-activated calcium channels globally. Scale bars, 65 ms and 34 μm . **k**, Currents recorded from W3B-RGCs (-60 mV) in response to stimulation of VG3-ACs at their somas (INL) or terminals (IPL) in control and CdCl₂ (200 μM) containing solution (left). Average peak current evoked by either soma (INL) or nerve terminal (IPL) stimulation in CdCl₂ solution expressed as a percentage of that found in control (right, $n = 276$ VG3-ACs and 5 W3B-RGCs). Currents evoked by IPL stimulation in CdCl₂-containing solution result from Ca²⁺ influx via ChR2 on VG3-AC terminals. VG3-ACs synapse directly with W3B-RGCs. **l**, Sample currents evoked in W3B-RGCs, W3D-RGCs and ooDSGCs by blue light (one-photon) stimulation of ChR2 positive VG3-ACs. Experiments were done in the presence of a cocktail of blockers: 10 μM ACET, to block the OFF pathway; 20 μM L-AP4, to block the ON pathway, and 300 μM hexamethonium, to block cholinergic nicotinic receptors^{19,51}. **m**, Average peak currents from experiments like those in **l** ($n = 15$ W3B-RGCs, $n = 7$ W3D-RGCs and $n = 13$ ooDSGCs). These results from one-photon stimulation of a population of VG3-ACs, confirm the conclusion from two-photon stimulation of single VG3-ACs (Fig. 2): these amacrine cells innervate W3B-RGCs far more strongly than W3D-RGCs or ooDSGCs. By one-photon stimulation, the currents evoked in ooDSGCs are stronger than those in W3D-RGCs, whereas they are similar in the two-photon data. This difference probably arises from their larger dendritic size. On the basis of the dendritic diameter of VG3-ACs (~ 50 μm ; Figs 2c and 3r), W3B-RGCs (~ 115 μm ; Figs 2c and 3l), W3D-RGCs (~ 125 μm ; data not shown) and ooDSGCs (200 μm ; ref. 37), we can estimate that dendrites of W3B-RGCs, W3D-RGCs and ooDSGCs overlap dendrites of ~ 24 , ~ 29 and ~ 100 VG3-ACs, respectively. Given the percentage connectivity in shown in Fig. 2, we estimate that each W3D-RGC is innervated by 10–15 VG3-ACs, whereas each ooDSGC is innervated by ~ 35 VG3-ACs.

a**b**

Extended Data Figure 5 | Synaptic connectivity of VG3-ACs and W3B-RGCs. **a, b,** Strength of connections as a function of distance from six interneuron types to W3B-RGCs (a) and VG3-ACs to four RGC types (b). Number of synaptic partners assayed shown above and sample currents shown below each graph. The W7 population contained six nearly-

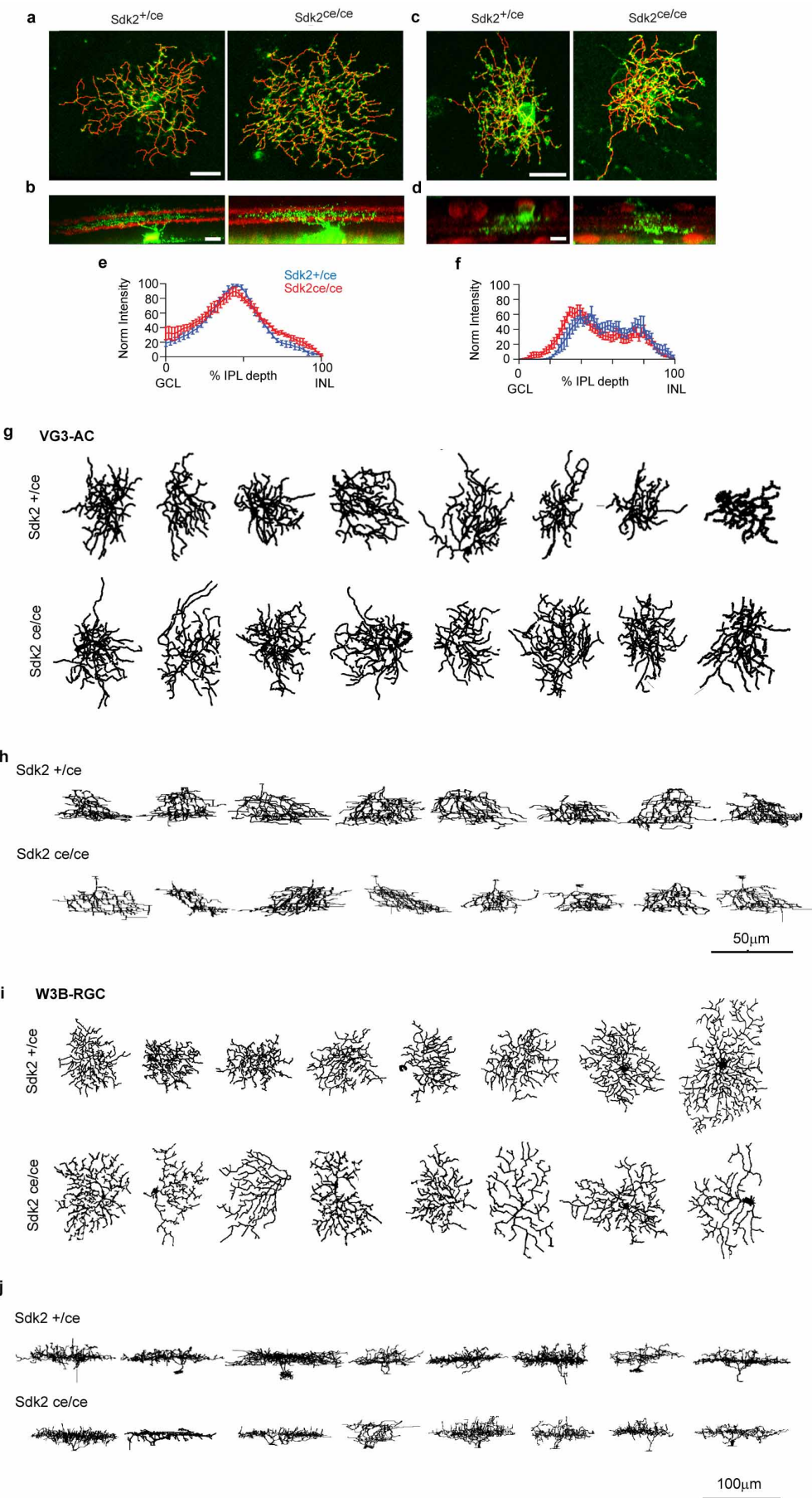
disconnected and ten connected pairs, presumably corresponding to the S1-laminating and S3-laminating W7 subsets. Normalized peak currents (I_{peak}) from each pair were normalized to the average maximum response from VG3-AC-W3B-RGCs.



Extended Data Figure 6 | Normal retinal architecture in *Sdk2* mutants.

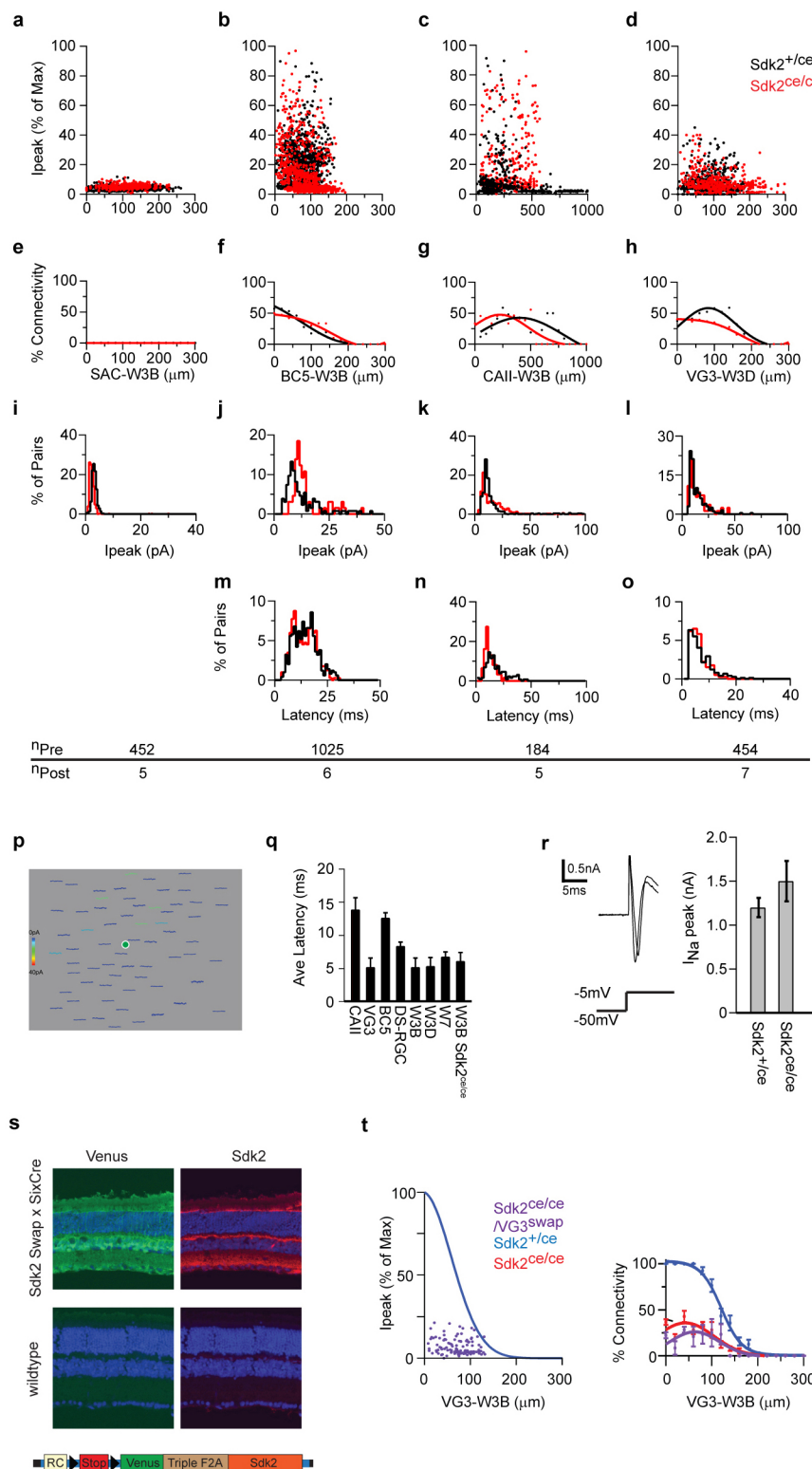
Sections of *Sdk2*^{ce/ce} and *Sdk2*^{ce/ce} retinas (P30) were stained with antibodies to cell-type-specific markers, synaptic components or fluorescent proteins. No differences between mutants and controls were detected in cells other than VG3-ACs and W3B-RGCs. **a**, Brn3a labels most RGCs. **b**, AP2 labels all amacrine cells. **c**, **d**, Synapsin I and SV2 are associated with synaptic vesicles. **e**, VGlut1 is concentrated in photoreceptor and bipolar terminals. **f**, PSD-95 family members, stained with anti-MAGUK, are associated with synaptic sites. **g**, Synaptotagmin 2 is concentrated in

bipolar cells types 2 and 6. **h**, Anti-HCN4 labels type 3a bipolar cells. **i**, Anti-disabled-1 (Dab1) labels AII amacrine cells. **j**, Anti-VACHT labels dendrites of SACs. **k**, Anti-calretinin labels subsets of RGCs and amacrine cells, including SACs. **l**, Anti-protein kinase C- α (PKC α) labels rod bipolar cells and a subset of amacrine cells. **m**, Anti-VGlut3 labels VG3-ACs. Sprouting is evident in the mutant. **n**, Single-cell reconstructions of VG3-ACs labelled sparsely with GFP in retinal cross-sections. **o**, Quantification of sprouting in mutant VG3-ACs. Scale bars, 10 μ m.



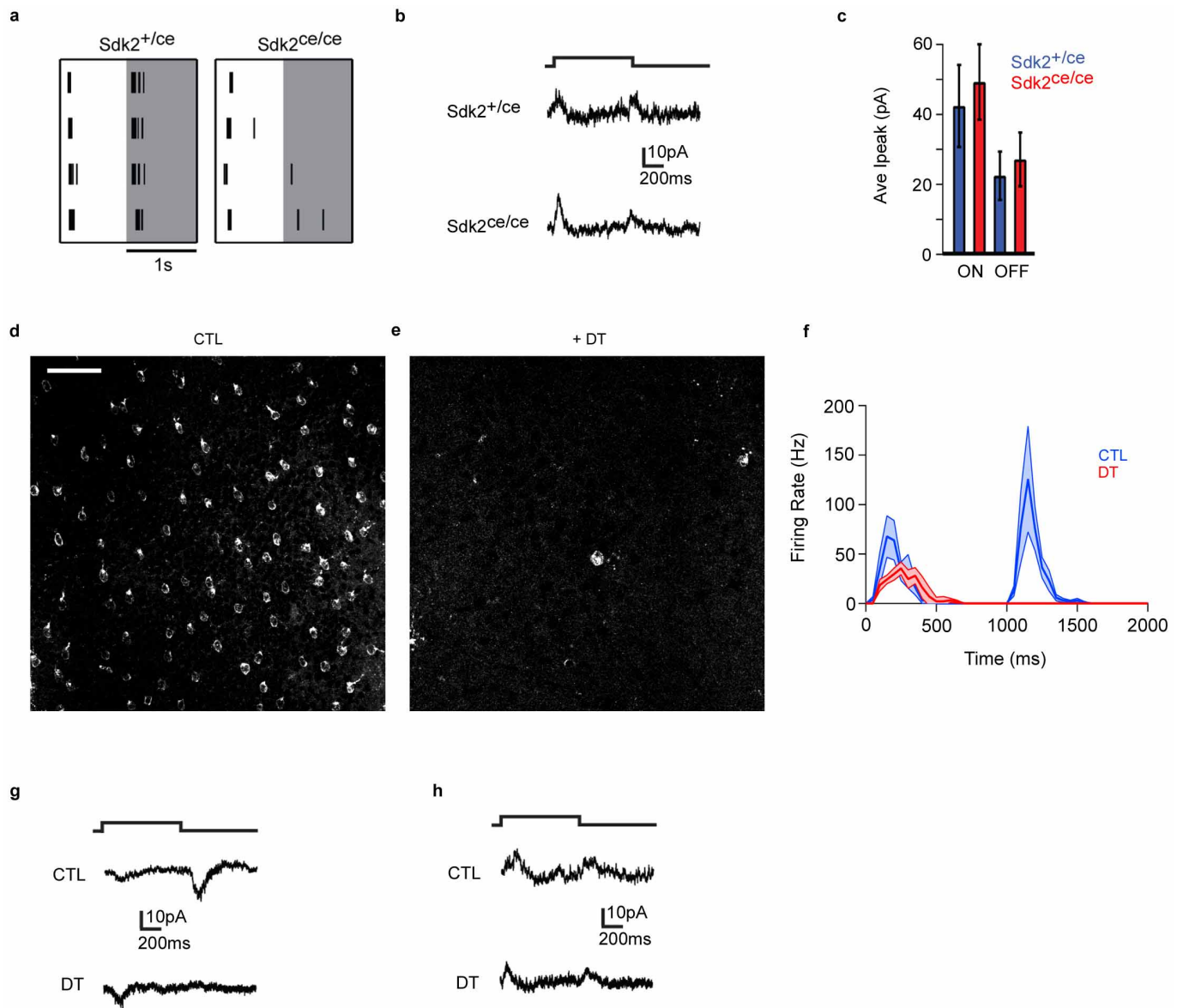
Extended Data Figure 7 | Morphological analysis of VG3-ACs and W3B-RGCs in *Sdk2* mutants. **a, b,** Dye-injected W3B-RGCs were imaged and skeletonized as described in Methods. Projections on rotated stacks counterstained with anti-VAcH_T antibodies are shown in **h**. **c, d,** Similar to **a, b**, except for VG3-ACs labelled sparsely with tdTomato and counterstained with anti-ChAT to label the somas of SACs. Scale bars, 25 μ m. **e, f,** Mean intensity

(\pm s.e.m.) of dye-labelled W3B-RGC dendrites (**e**) and VG3-AC dendrites (**f**) across the IPL from images such as those shown in **a–d**. **g, h,** En face or laminar projections of skeletonized dendritic arbors from VG3-ACs labelled sparsely with tdTomato in *Sdk2*^{+/ce} and *Sdk2*^{ce/ce} retinae. **i, j,** En face or laminar projections of skeletonized dendritic arbors from dye-filled W3B-RGCs in *Sdk2*^{+/ce} and *Sdk2*^{ce/ce} retinae.



Extended Data Figure 8 | Electrical and synaptic properties of *Sdk2* mutant VG3-ACs and W3B-RGCs. **a–l**, Strength of connections as a function of distance from three interneuron types (SACs, type 5 bipolar cells (BC5) and type II catecholaminergic cells (CAII)) to W3B-RGCs and from VG3-ACs to W3D-RGCs in *Sdk2*^{ce/+} (black) and *Sdk2*^{ce/ce} (red) retinae. **a–d**, Normalized peak current. **e–h**, Percentage of connected pairs. **i–l**, Average current amplitudes in a 30-ms window after the stimulus pulse. **m–o**, Latencies of currents detectable above noise. Number of pre- and postsynaptic partners assayed shown below each column. **p**, Responses evoked in a W3B-RGC (green dot) in a *Sdk2* mutant after stimulation of 66 VG3-ACs (genotype: TYW3; *Sdk2*^{ce/ce}; *Vglut3-cre*; *LOX-STOP-LOX-ChR2-tdTomato*). **q**, Average latencies

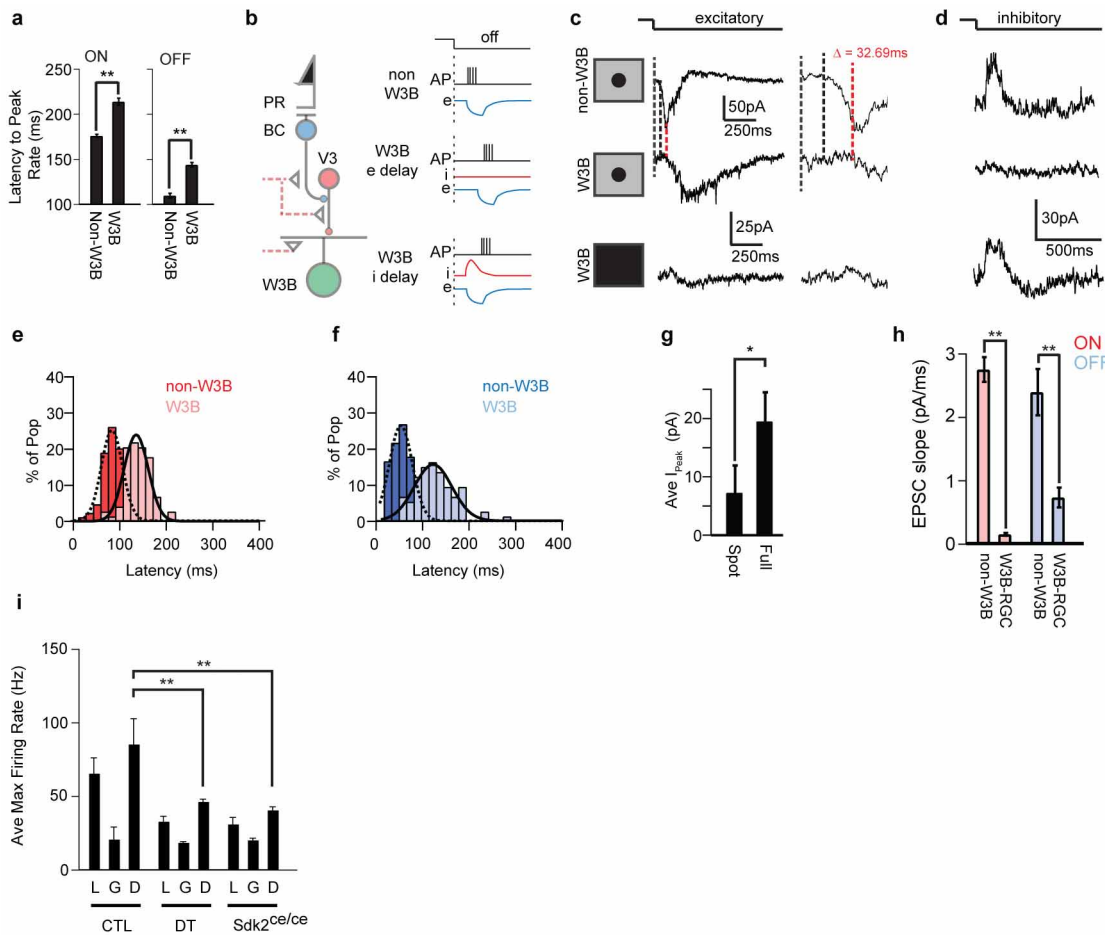
for currents detectable above noise in control. **r**, Sodium currents in W3B-RGCs *Sdk2*^{ce/+} and *Sdk2*^{ce/ce} retinae. Sample currents evoked by a step from -60 mV to -5 mV (left), and average peak sodium current amplitude measured on W3B-RGCs in *Sdk2*^{ce/+} and *Sdk2*^{ce/ce} retinae. **s**, Retinal cross-sections from wild-type mice and those that overexpress *Sdk2* broadly using the *Six3-cre* driver and the *Sdk2* swap transgene. *Sdk2* is expressed strongly from the swap transgene, which is shown as a schematic below the micrographs. **t**, Strength of connections from VG3-ACs to W3B-RGCs in *Sdk2*^{ce/ce} mutants in which *Sdk2* expression was rescued in VG3-ACs. Data were derived from 121 VG3-ACs and 3 W3B-RGCs. Fit to the control data (Fig. 3a) re-plotted in blue.



Extended Data Figure 9 | Effective deletion of VG3-ACs by diphtheria toxin. **a**, Spike responses of W3B-RGCs in $Sdk2^{ce/+}$ and $Sdk2^{ce/ce}$ retinas in response to a ~100-μm flashing spot centred on the receptive field. OFF responses are strongly reduced in the absence of Sdk2. **b**, Inhibitory currents recorded ($V_h = -5$ mV) from W3B-RGCs in $Sdk2^{+/ce}$ and $Sdk2^{ce/ce}$ retinas in response to a full field flash for 1 s. **c**, I_{peak} measured from excitatory currents in non-W3B-RGCs ($n = 8$ in 4 $Sdk2^{ce/+}$ mice and 8 in 4 $Sdk2^{ce/ce}$ mice).

d, e, Sample images of tdTomato-positive VG3-ACs in retinas from diphtheria-toxin-treated control (**d**) and $Vglut3\text{-}cre; Rosa\text{-}CAG\text{-}LOX\text{-}STOP\text{-}LOX\text{-}DTR}$

mice (**e**). Scale bar, 40 μm. **f**, Average firing rate recorded from W3B-RGCs in control (blue, $n = 21$) and diphtheria-toxin-treated $Vglut3\text{-}cre; DTR/TYW3$ (red, $n = 12$) retinas in response to small spots flashed for 1 s. Dark lines, average; shadowing denotes s.e.m. Bin width, 50 ms. **g**, Excitatory currents recorded ($V_h = -65$ mV) from W3B-RGCs in control and diphtheria-toxin-treated $Vglut3\text{-}cre; DTR/TYW3$ retinas in response to small spots flashed for 1 s. **h**, Inhibitory currents recorded ($V_h = -5$ mV) from W3B-RGCs in control and diphtheria-toxin-treated $Vglut3\text{-}cre; DTR/TYW3$ retinas in response to small spots flashed for 1 s.



Extended Data Figure 10 | A delay line in the differential motion response. **a**, Average latency to peak firing rate in W3B-RGCs and non-W3B-RGCs in response to a spot flashed over their receptive field centre ($n = 21$ non-W3B-RGCs and 18 W3B-RGCs). Spike responses on W3B-RGCs are delayed (** $P < 0.01$, Student's t -test). **b**, Possible mechanisms for the delay. In non-W3B-RGCs excitatory currents produced by bipolar cells drive the neuron to fire. In W3B-RGCs, spikes could be delayed because the interposition of VG3-ACs delays the onset of the excitatory postsynaptic current (EPSC) (W3B e delay) or because of a transient inhibitory postsynaptic current that arrives at the same time as the EPSC and delays the cell from reaching threshold (W3B i delay). **c**, **d**, Excitatory (**c**) and inhibitory (**d**) currents measured from non-W3B-RGCs and W3B-RGCs in response to a flashing spot centred on the receptive field or a full field flash. Dotted lines denote the stimulus onset, non-W3B-RGC EPSC onset and W3B-RGC EPSC onset (red). The onset of EPSCs in W3B-RGC lags behind those found in non-W3B-RGCs by ~30 ms. No significant transient inhibition was observed in the receptive field centre (**d**). **e**, **f**, Histogram of latency to the onset of the ON (**e**) and OFF (**f**) excitatory

current measured on W3B-RGCs (light blue, light red) and non-W3B-RGCs (blue, red). W3B-RGCs lag non-W3B-RGCs by ~32–40 ms and also have higher variance about the mean ($n = 29$ non-W3B-RGCs and 27 W3B-RGCs). **g**, Average peak of inhibitory currents measured on W3B-RGCs in response to a ~100- μ m diameter flashing spot and a full field flash ($n = 6$ wild-type W3B-RGCs; * $P < 0.05$, Student's t -test). **h**, Slope of the light-evoked excitatory current between 10% and 90% of the peak. Slopes of currents in W3B-RGCs are significantly lower than those of non-W3B-RGCs ($n = 29$ non-W3B-RGCs and 27 W3B-RGCs; ** $P < 0.001$). The non-W3B-RGCs included W3D-RGCs, ooDSGCs, α -RGCs and some unidentified RGCs. **i**, Average maximal firing rates measured in W3B-RGCs to local, global and differential motion stimuli ($n = 10$ W3B-RGCs in 5 control mice, 6 W3B-RGCs in 4 $Sdk2^{ce/ce}$ mice and 9 W3B-RGCs in 3 diphtheria-toxin-treated *Vglut3-cre;DTR/TYW3* mice; ** $P < 0.01$, Student's t -test). Firing rates in global and differential motion were normalized to that elicited in control W3B-RGCs with local motion stimuli for Fig. 4j.